Evaluation of Hybrid GSC-based and ASSB-based Beamforming Methods Applied to Ultrasound Imaging

by

Mohammed Bani M. Albulayli
B.Sc., King Saud University, 2005

A Thesis Submitted in Partial Fulfillment
of the Requirements for the Degree of

MASTER OF APPLIED SCIENCE

in the Department of Electrical and Computer Engineering

Supervisory Committee

Evaluation of GSC-based and ASSB-based Beamforming Methods Applied to Ultrasound Imaging

by

Mohammed Bani M. Albulayli
B.Sc., King Saud University, 2005

Supervisory Committee

Dr. Daler Rakhmatov, Department of Electrical and Computer Engineering

Supervisor

Dr. Panajotis Agathoklis, Department of Electrical and Computer Engineering

Departmental Member

Abstract

Supervisory Committee

Dr. Daler Rakhmatov, Department of Electrical and Computer Engineering

Supervisor

Dr. Panajotis Agathoklis, Department of Electrical and Computer Engineering

Departmental Member

The application of adaptive beamforming to biomedical ultrasound imaging has been an active research area in recent years. Adaptive beamforming techniques have the capability of achieving excellent resolution and sidelobe suppression, thus improving the quality of the ultrasound images. This quality improvement, however, comes at a high computational cost. The work presented in this thesis aims to answer the following basic question: Can we reduce the computational complexity of adaptive beamforming without a significant degradation of the image quality? Our objective is to explore a combination of low-complexity non-adaptive beamforming, such as the conventional Delay-and-Sum (DAS) method, with high-complexity adaptive beamforming, such as the standard Minimum-Variance Distortionless Response (MVDR) method implemented using the Generalized Sidelobe Canceller (GSC). Such a combination should have the lower computational complexity than adaptive beamforming, but it should also offer the image quality comparable to that obtained using adaptive beamforming. In addition to the adaptive GSC-based MVDR beamforming method, we also investigate the performance

of the so-called Adaptive Single Snapshot Beamformer (ASSB), which is relatively unexplored in the ultrasound imaging literature.

The main idea behind our approach to combining a non-adaptive beamformer with an adaptive one is based on the use of the data-dependent variable known as the coherence factor. The resulting hybrid beamforming method can be summarized as follows: For each input snapshot to be beamformed, calculate the corresponding coherence factor; if the coherence factor is below a certain threshold, use non-adaptive DAS beamforming, otherwise use adaptive (GSC-based or ASSB-based) beamforming. We have applied this simple switching scheme to the simulated B-mode ultrasound images of the 12-point and point-scatterer-cyst phantoms that are commonly used in the ultrasound imaging literature to evaluate the image quality. Our simulation results show that, in comparison to optimal high-complexity always-adaptive beamforming, our hybrid beamformer can yield significant computational savings that range from 59% to 99%, while maintaining the image quality (measured in terms of resolution and contrast) within a 5% degradation margin.

Table of Contents

Supervisory Committee ii

Abstract iii

Table of Contents v

List of Tables vi

List of Figures vii

Acknowledgments xi

Dedication xii

List of Acronyms xiii

Chapter 1: Introduction 1

Chapter 2: Background 6

2.1 Ultrasound System 6

2.2 Ultrasound Image Quality 8

2.3 MVDR Beamforming 10

2.3.1 Spatial Smoothing 12

2.3.2 Coherence Factor 12

2.3.3 Baseline Simulated Images 13

2.4 Related Work 18

2.4 Our Contribution 21

Chapter 3 Hybrid GSC-based Beamforming 23
3.1 GSC Beamforming..... 23
3.2 Proposed Method 25
3.3 Computational Complexity Analysis 27

Chapter 4 Hybrid ASSB-based Beamforming 30
4.1 Introduction..... 30
4.2 Adaptive Single Snapshot Beamforming 32
4.3 Proposed Method 35
4.4 Computaional Complexity Analysis 38

Chapter 5: Evaluation Results..... 41
5.1 Hybrid GSC-Based Beamforming..... 41
5.2 Hybrid ASSB-Based Beamforming..... 51

Chapter 6: Conclusion and Future Work..... 60
6.1 Conclusion 60
6.2 Future Work 62

Bibliography..... 63

Appendix A..... 70
FIELD-II Simulation Tool... 70

List of Tables

Table 3.1: Computational cost of each GSC-based beamforming step……. 29

Table 4.1: Computational cost of each ASSB-based beamforming step……... 40

Table 5.1: Hybrid GSC-based beamforming: computational savings in comparison to fully adaptive GSC-based beamforming…….. 42

Table 5.2: Hybrid GSC-based beamforming: FWHM, sidelobe energy E_{SL}, and mainlobe energy E_{ML} at the transmit focus (12-point phantom)…….. 43

Table 5.3: Hybrid GSC-based beamforming: contrast with respect to the speckled background (point-scatterer-cyst phantom)…….. 46

Table 5.4: Hybrid ASSB-based beamforming: computational complexity in our test example compared to fully adaptive ASSB-Based beamforming…. 51

Table 5.5: Hybrid ASSB-based beamforming: FWHM, sidelobe energy E_{SL}, and Mainlobe energy E_{ML} at the transmit focus (12-point phantom)…….. 53

Table 5.6: Hybrid ASSB-based beamforming: contrast with respect to the speckled background (point-scatterer-cyst phantom)……... 55

Table 6.1: 12-point phantom: performance summary of DAS, always-adaptive GSC recommended hybrid GSC, always-adaptive ASSB, and recommended hybrid ASSB beamforming…….. 61

Table 6.1: Point-scatterer-cyst phantom: performance summary of DAS, always-adaptive GSC recommended hybrid GSC, always-adaptive ASSB, and recommended hybrid ASSB beamforming…….. 61

List of Figures

Figure 1.1: Typical ultrasound system……... 2

Figure 1.2: Delay-and-sum beamformer……...…..…… 3

Figure 2.1: Performance of rectangular-windowed DAS (left), Kaiser-windowed DAS (center), and MVDR (right) beamforming without CF scaling: 12-point phantom, point placement in 10-mm intervals, 64 scan lines, 4-MHz 98-element phased array transducer (transmit focus at 60 mm, dynamic receive focus at 10 mm intervals), spatial smoothing with L = 49 and N = 1……. 15

Figure 2.2: Performance of rectangular-windowed DAS (left), Kaiser-windowed DAS (center), and MVDR (right) beamforming with CF scaling: 12-point phantom, point placement in 10-mm intervals, 64 scan lines, 4-MHz 98-element phased array transducer (transmit focus at 60 mm, dynamic receive focus at 10 mm intervals), spatial smoothing with L = 49 and N = 1……. 16

Figure 2.3: From top to bottom: performance of rectangular-windowed DAS, Kaiser-windowed DAS, MVDR (all three without CF scaling), rectangular-windowed DAS, Kaiser-windowed DAS, and MVDR (all three with CF scaling) beamforming: Point-scatterer-cyst phantom placed at 60 mm (lateral placement: single point at −15 mm, 3-mm scattering region at −5 mm, 4-mm water-filled cyst at 10 mm), 64 scan lines, 4-MHz 192-element linear array transducer (66 active elements, transmit focus at 60 mm, dynamic receive focus at 10 mm intervals), spatial smoothing with L = 33, using N = 2…… 17

Figure 3.1: Generalized sidelobe canceller……..…….... 24

Figure 4.1: *K* source signals incident on uniform linear array *M* sensors.. 31

Figure 4.2: Adaptive single snapshot beamformer structure……..…… 34

Figure 5.1: Hybrid GSC-based beamforming: PSF at transmit focus 60 mm..... 44

Figure 5.2: Sampled areas used for contrast computations: point scatterer-cyst phantom obtained using DAS beamforming.……. 45

Figure 5.3: From left to right: 12-point phantom image obtained using DAS, fully adaptive GSC, and hybrid GSC with T_{CF} = 0.01…….…..…... 47

Figure 5.4: From left to right: 12-point phantom image obtained using hybrid GSC with TCF = 0.05, hybrid GSC with T_{CF} = 0.1, and hybrid GSC with T_{CF} = 0.15……...…….. 48

Figure 5.5: From top to bottom: point-scatterer-cyst phantom image obtained using DAS, always-adaptive GSC, and hybrid GSC with T_{CF} = 0.01…… 49

Figure 5.6: From top to bottom: point-scatterer-cyst phantom image obtained using hybrid GSC with T_{CF} = 0.05, hybrid GSC with T_{CF} = 0.1, and hybrid GSC with T_{CF} = 0.15……..…… 50

Figure 5.7: Hybrid ASSB-based beamforming: PSF at transmit focus 60 mm……...… 54

Figure 5.8: From left to right: 12-point phantom image obtained using always-adaptive ASSB, hybrid ASSB with T_{CF} = 0.01, and hybrid ASSB with T_{CF} = 0.05…….……. 56

Figure 5.9: From left to right: 12-point phantom image obtained using hybrid ASSB with T_{CF} = 0.1, and hybrid ASSB with T_{CF} = 0.15……..……..... 57

Figure 5.10: From top to bottom: point-scatterer-cyst phantom image obtained using always-adaptive ASSB, hybrid ASSB with T_{CF} = 0.01, and hybrid ASSB with T_{CF} = 0.05…… 58

Figure 5.11: From top to bottom: point-scatterer-cyst phantom image obtained using hybrid ASSB with T_{CF} = 0.1 and hybrid ASSB with T_{CF} = 0.15…..……... 59

Acknowledgements

First and foremost, I would like to express my most sincere gratitude to my supervisor Dr. Daler Rakhmatov for his encouragement, support and guidance throughout the course of my master's program. Further, I thank Dr. Panajotis Agathoklis (my supervisory committee member) and Dr. Daniela Constantinescu (my external examiner) for their help with improving my thesis. Finally, I would like to express my sincere appreciation to the Ministry of Higher Education in Saudi Arabia and the Saudi Arabian Cultural Bureau in Canada for providing financial support during my graduate studies at the University of Victoria.

Dedication

To My Parents (Ghaytha Alzuhairi and Bani Albulayli),

For their endless love, support and encouragement

List of Acronyms

Analog-to-Digital Converter	ADC
Adaptive Single Snapshot Beamforming	ASSB
Coherence Factor	CF
Digital-to-Analog Converter	DAC
Delay and Sum [Beamforming]	DAS
FLoating-point OPeration	FLOP
Full Width at Half Maximum	FWHM
Generalized Sidelobe Canceller [Beamforming]	GSC
High Voltage [Amplifier]	HV
Linearly Constrained Minimum Variance [Beamforming]	LCMV
Low Noise Amplifier	LNA
Minimum Variance Distortionless Response [Beamforming]	MVDR
Point Spread Function	PSF
Signal-to-Interference plus Noise Ratio	SINR
Signal-to-Noise-Ratio	SNR
Time Gain Compensation	TGC

Chapter 1

Introduction

Medical ultrasound is widely used as a diagnostic tool in medical clinics due to its safety, portability, relative low cost and non-invasiveness nature compared to other imaging modalities. A typical medical ultrasound imaging system employs an array of piezoelectric sensors. In order to obtain an image, focused short sound pulses are sent to the desired region, and then the received echoes from different tissues in that region are processed using array signal processing algorithms, as shown in Figure 1.1 and discussed in Chapter 2 (see Section 2.1). The focus of this thesis is on the *receive beamforming* block of Figure 1.1 [1, 44].

In its simplest form, the receive beamforming block delays and sums the received signals as shown in Figure 1.2. The set of the time delays $\tau_1, \tau_2, \dots, \tau_M$ is used to focus the received data: these delays are determined based on the distance travelled by a reflected ultrasound wave from the region of interest to a particular sensor of the transducer array, relative to a certain reference position (usually, the center of the array). Each focused signal from the *input vector* $x_1[n], x_2[n], \dots, x_M[n]$ is multiplied by the corresponding beamforming weight $w_1[n], w_2[n], \dots, w_M[n]$ and these products are then summed to produce the output signal $y[n]$. The set of weights, or the *weight vector*, can be either fixed (data-independent), or adaptive (data-dependent). The fixed weights are commonly realized by means of standard window functions, e.g., the rectangular, Hamming, or Kaiser window. The choice of a particular window depends on a desired balance between the mainlobe width and the sidelobe level, which translates into a

balance between the image resolution and contrast [3, 4]. There is a fundamental tradeoff between the image contrast and resolution: reducing the sidelobe level gives rise to a wider mainlobe width and vice versa.

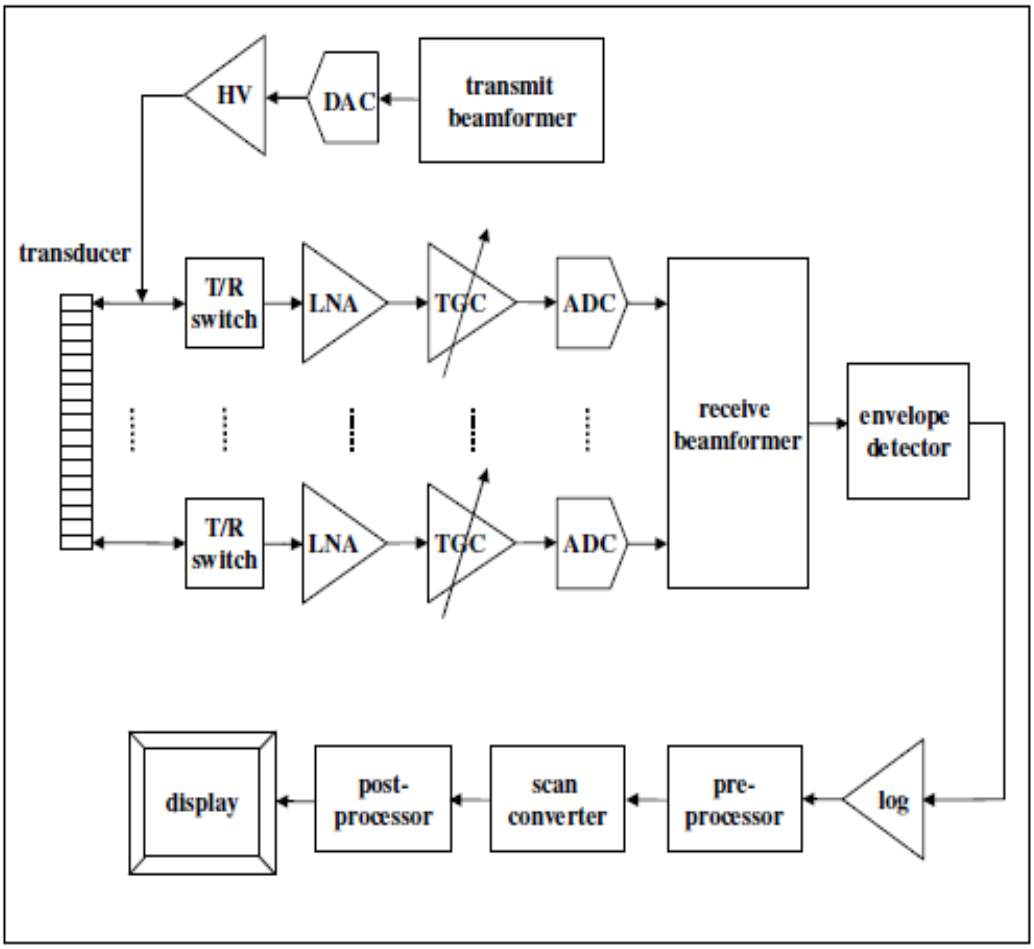

Figure 1.1: Typical ultrasound system [1,44].

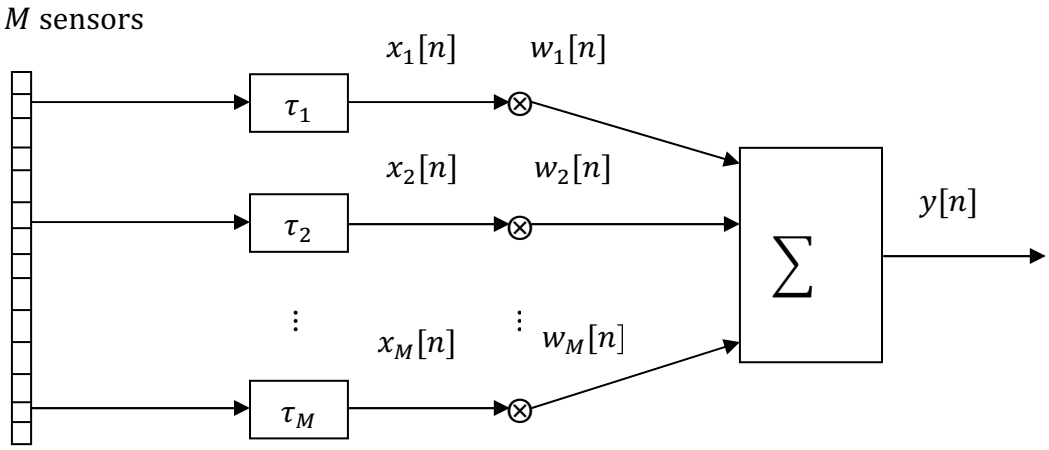

Figure 1.2: Delay-and-sum beamformer.

Adaptive beamforming can achieve a narrow mainlobe width and at the same time suppress the sidelobe level, thus improving both the image resolution and contrast in comparison to fixed beamforming. However, such an improvement comes at a significant computational cost, as the data-dependent adaptive weight vector must be continuously recalculated based on the characteristics of each received input vector. The adaptive beamforming weights are also dependent on the choice of a criterion that preserves the desired signal while rejecting the unwanted interference and noise. In this thesis we employ the well-known *minimum variance distortionless response* (MVDR) criterion. It is based on the second-order statistics (the estimated covariance matrix) of the input data, and it requires the output power be minimized while passing a signal in the desired look-direction with unity gain. In other words, the MVDR beamformer passes the desired on-axis signal undistorted, while suppressing the undesired off-axis signals. The application of the MVDR beamformer to ultrasound imaging has been extensively reported in the literature, demonstrating significant improvements in the image resolution and contrast. However, calculating adaptive MVDR weights involves a matrix inversion operation performed for each received input vector, which is computationally expensive.

The main motivation behind our work is to address the problem of a high computational load imposed by adaptive beamforming on the ultrasound system. Our objective is to reduce the computational cost of beamforming toward that of a non-adaptive beamformer, while retaining the quality of beamforming comparable to that of an adaptive beamformer. Our approach is based on the following simple idea. We switch between a non-adaptive beamformer and an adaptive one based on the value of the data-dependent variable known as the *coherence factor*. The resulting hybrid beamformer works as follows. For each input vector, we calculate the corresponding coherence factor. If the coherence factor is below a certain threshold, we use non-adaptive *delay-and-sum* (DAS) beamforming; otherwise, we use adaptive beamforming. To implement adaptive MVDR beamforming, we use the well-known *Generalized Sidelobe Canceller* (GSC). In addition to the adaptive GSC-based beamforming method, we also investigate the performance of the so-called *Adaptive Single Snapshot Beamformer* (ASSB), which is relatively unexplored in the ultrasound imaging literature. The ASSB is related to the *maximum signal-to-noise and interferer ratio* (SNIR) beamforming criterion, but without the knowledge of the noise and signal correlation matrices [42].

We have applied our simple switching scheme to the simulated B-mode ultrasound images of the 12-point and the point-scatterer-cyst phantoms, generated by the FIELD-II simulation tool and commonly used in the ultrasound imaging literature to evaluate the image quality. Our simulation results show that, in comparison to (optimal but expensive) always-adaptive beamforming, our hybrid beamformer yields significant computational savings between 59% and 99%, yet the image quality degradation (measured in terms of the image resolution and contrast) is below 5%.

To summarize, this thesis makes the following contributions to the ultrasound imaging literature:

- We apply the *hybrid GSC-based beamforming* method to ultrasound imaging and evaluate its performance using several switching thresholds associated with the coherence factor of the received input vectors.

- We apply the *hybrid ASSB-based beamforming* method to ultrasound imaging and evaluate its performance using several switching thresholds associated with the coherence factor of the received input vectors.
- We estimate and quantitatively compare the computational costs of the hybrid GSC-based and ASSB-based beamformers to those of their always-adaptive counterparts, thus exposing the *quality-cost tradeoffs* that are enabled by hybrid beamforming.

The rest of the thesis is organized as follows. Chapter 2 provides a brief overview of a typical biomedical ultrasound imaging system, introduces the MVDR beamforming and coherence factor concepts, and also discusses the previous work related to this thesis. Chapter 3 presents the hybrid GSC-based beamformer and its computational complexity analysis, while Chapter 4 presents the hybrid ASSB-based beamformer and its computational complexity analysis. Chapter 5 provides our FIELD-II simulation results, compares the quality of the simulated images obtained by our beamformers under investigation, and discusses the computational savings due to the hybrid beamforming approach. Finally, in Chapter 6 we state our conclusions and outline several ideas for future work.

Chapter 2

Background

This chapter provides a brief overview of a typical biomedical ultrasound imaging system, introduces the MVDR beamforming and coherence factor concepts, and also discusses the previous work related to this thesis.

2.1 Ultrasound System

The focus of this thesis is on the two-dimensional brightness-mode (B-mode) imaging, in which the displayed pixel brightness is a function of the amplitude of the returning echoes. Figure 1.1 shows a typical B-mode ultrasound system, whose basic components are described in the sequel.

Acoustic waves of frequencies beyond 20 kHz are referred to as ultrasound waves. Typically, ultrasound system works on frequencies that range from 2 MHz to 20 MHz [2]. During transmission, piezoelectric transducer elements are excited by electric pulses to produce sound waves whose echoes are used to form an image. As the number of elements increases, the sensitivity and spatial resolution are improved. The inter-element spacing should be less than or equal to half of the wavelength in order to suppress the grating lobes. The grating lobes occur in symmetric locations around the mainlobe and with the same amplitude. The grating lobes cause imaging artifacts and reduce the image contrast [2, 3]. The B-mode ultrasound imaging system uses one-dimensional array of

transducers to produce two-dimensional images. There are several ways of acquiring ultrasound images, the most popular ones utilizing a linear array or a phased array of transducer elements [1]. Focusing and steering the ultrasound beam play an important role in the beamforming process. During the transmission, only fixed focusing is allowed [3], whereby for every scan line certain time delays are applied to the transmitting transducers. These time delays depend on the focal point and the steering angle. Every signal from every transducer takes a different time to arrive at the focal point. The time needed depends on the location of the transducer from the center of the array and the speed of sound at the medium in which the focal point lies. Therefore, appropriate time delays are needed to compensate for the time differences, in order to equalize the phases of the transmitted signals at the time of their arrival to the focal point. Usually, the speed of sound is assumed to be 1540 m/s through soft tissues, however, the speed of sound can deviate by approximately ± 5% which may increase the mainlobe width by as much as 300% [3]. After this focusing step, the output signals of the transmitting beamforming are converted to analog signals by the digital to analog converter (DAC) and passed through high voltage (HV) amplifiers that drive the transducers [2].

At the receiving side the reflected echoes pass through the transmit and receive (T/R) switches that isolate the HV amplifiers from damaging the received echoes. The T/R switches are followed by low noise amplifiers (LNA) to improve the signal-to-noise ratio (SNR) of the returning echoes [1]. Then, the echoes pass through time gain compensation (TGC) amplifiers needed due to the fact that some of the returning echoes are attenuated differently depending on their propagation depth. The resulting analog signals are converted to digital signals using analog-to-digital converter (ADC) and then supplied to a receive beamformer, where dynamic focusing is allowed [3].

After beamforming the received echoes, we need to extract the envelope of the beamformer output. This is accomplished by applying and taking the absolute values of the Hilbert transform of the beamformer output [7]. Next, the estimated envelope is appropriately decimated to match the time and the distance scales. Then, a logarithmic compression takes place to reduce the dynamic range of the received data [3]. The resulting data is not yet suitable for screen display: it has to be interpolated, that is, spatially remapped. This process is accomplished via the scan converter [1]. Before

displaying the output image, a step known as a post-processing stage occurs. In this stage several non-linear curves can be selected by the operator are chosen to highlight high- or low-amplitude echoes pertaining to the scan under view. This affects the final gray-scale image mapping, and hence the perceived dynamic range of the output image [1].

The quality of ultrasound images is greatly affected by the presence of noise. There are two types of noise in ultrasound systems. The first one is the Gaussian white noise which is resulted from the electronic components of the system. The second type is speckle noise. Speckle noise is the grainy appearance of a homogenous tissue in ultrasound image [3]. It is an undesirable phenomenon, as it decreases the contrast resolution thus obscuring boundaries between tissues inside the human body. The speckle noise is caused by the constructive and destructive of the interferences of the echoes scattered and reflected by the microscopic structures whose sizes are comparable to the wavelength of the incident ultrasound waves [1]. Speckle noise is not strictly random, but rather an intrinsic property of the tissues to be imaged [8].

2.2 Ultrasound Image Quality

This section summarizes some of the important quantitative factors used to assess the quality of ultrasound images.

Spatial Resolution

The spatial resolution measures the ability of the beamformer to distinguish closely spaced objects. The spatial resolution can be divided into two types the lateral and axial resolutions.

The *axial resolution* measures the ability of the beamformer to distinguish objects that lie on the direction of ultrasound wave propagation. It depends on the duration of the transmitted pulse and the speed of sound [6]:

$$R_{axial} = \frac{cM}{2f_0} = \frac{\lambda M}{2} \tag{2.1}$$

where M is the number of periods of the transmitted sinusoidal wave, whereas c, f_0 and λ are the speed, frequency and the wavelength of the transmitted sound wave, respectively. The factor 2 accounts for the round trip delay of the pulse. As can be seen from equation (2.1), the higher the frequency (or the shorter the pulse) leads to greater axial resolution. Increasing the frequency, however, leads to increased attenuation [1]. Hence, the axial resolution is typically limited by the pulse length.

The *lateral resolution* measures the ability of the beamformer to distinguish objects that are perpendicular to the direction of ultrasound propagation. It depends on the width of the active transducers [6]:

$$R_{3dB} = \frac{\lambda z}{D} = \lambda F\# \tag{2.2}$$

where

z is the distance to the imaged region,

D is the width of the active transducers,

$F\# = \frac{z}{D}$ is the *F*-number of the imaging system.

Contrast

The contrast is defined as follows [3]:

$$\text{Contrast} = \frac{S_{out} - S_{in}}{S_{out}} \tag{2.3}$$

where S_{out} is the average signal measured outside the region of interest, and S_{in} is the average signal measured at inside the region of interest. The major cause of the contrast degradation of the contrast factor is the sidelobes and grating lobes.

Frame Rate

In B-mode ultrasound system, high frame rate (usually, 20-100 frames per second) is required in order to capture the fast moving parts inside the body [6]. Since the image is produced by combining the echoes from a large number of scan lines, increasing the scan line density (thus increasing the frame rate) improves the lateral resolutions. However, if we want to increase the depth of field, we need to either decrease the frame rate, or to decrease the number of scan lines. These three parameters are related as follows:

$$F_{rate} \times z \times N_l = \frac{c}{2} \tag{2.4}$$

where F_{rate} is the frame rate in frames/second, and N_l is the number of scan lines.

2.3 MVDR Beamformer

At each time instance *n*, let an array of *M* transducer elements supply a focused input vector $\mathbf{x}[n]$ that needs to be beamformed to produce an output $y[n]$. The simplest non-adaptive beamforming method is called *delay-and-sum*, or DAS, where

$$y[n] = (x_1[n]\ e^{-j\frac{2\pi}{\lambda}d\sin(\theta_1)} + x_2[n]\ e^{-j\frac{2\pi}{\lambda}2d\sin(\theta_1)} + \ldots + x_M[n]\ e^{-j\frac{2\pi}{\lambda}Md\sin(\theta_1)})/M,$$

and parameters d and θ_1 are illustrated in Figure 4.1. Alternatively, we can use an adaptive beamformer, whose weights are determined based on the certain properties of the input vector. In this thesis we focus on the *minimum variance distortionless response* (MVDR) adaptive beamformer, whose output $y[n]$ and output power $P[n]$ are given by

$$y[n] = \mathbf{w}^H[n]\mathbf{x}[n] \tag{2.5}$$

$$P[n] = E\left\{|y[n]|^2\right\} = \mathbf{w}^H E\left\{\mathbf{x}[n]\mathbf{x}^H[n]\right\}\mathbf{w} = \mathbf{w}^H\mathbf{R}[n]\mathbf{w} \tag{2.6}$$

where $\mathbf{w}$ is the optimum weight vector of length $M \times 1$, $\mathbf{x}[n]$ is the input vector of length $M \times 1$, and $\mathbf{R}[n]$ is the covariance matrix of size $M \times M$. The objective and constraints of the MVDR beamformer can be expressed as follows:

$$\min_{\mathbf{w}} \mathbf{w}^H \mathbf{R}[n]\mathbf{w}, \text{ subject to } \mathbf{w}^H \mathbf{a} = 1 \tag{2.7}$$

where $\mathbf{a}$ is the $M \times 1$ steering vector of the desired signal. In other words, the MVDR beamformer minimizes the output power, while allowing the desired signal to pass undistorted (with a unity gain). The solution to the above optimization problem is given by [5]:

$$\mathbf{w}[n] = \frac{\mathbf{R}^{-1}[n]\mathbf{a}}{\mathbf{a}^{\mathbf{H}}\mathbf{R}^{-1}[n]\mathbf{a}} \tag{2.8}$$

In practice, however, the covariance matrix $\mathbf{R}[n]$ is not known and must be estimated as

$$\hat{\mathbf{R}}[n] = \frac{1}{N}\sum_{i=n-N}^{n} \mathbf{x}[i]\mathbf{x}^H[i] \tag{2.9}$$

where $\hat{\mathbf{R}}[n]$ is sample covariance matrix, $\mathbf{x}[i]$ is the i-th snapshot, and N is the number of the snapshots taken. As ultrasound signals are non-stationary, $\hat{\mathbf{R}}[n]$ changes rapidly over time; hence, the number of taken snapshots N is typically very small. More importantly, the received ultrasound echoes are correlated, leading to an ill-conditioned $\hat{\mathbf{R}}[n]$, which compromises MVDR beamforming quality. In a multipath ultrasound environment, the interferers are likely to be correlated, or coherent, with the desired signal (i.e., the interferers are scaled and shifted copies of the desired signal). As the MVDR beamformer passes the desired signal with a unity gain, it will also pass the coherent interferers that may cancel the desired signal altogether [11]. To resolve this problem, one can use spatial smoothing [9, 10] discussed next.

2.3.1 Spatial Smoothing

Shan and Kailath in [9] proposed a pre-processing step, known as spatial smoothing, whose purpose is to restores the rank of $\hat{\mathbf{R}}[n]$ in a coherent environment. We divide the array of M sensors into P overlapping subarrays of length $L = \frac{M}{2}$ (L may not exceed $\frac{M}{2}$). Letting $\mathbf{x}_p[n] = [x_p[n], x_{p+1}[n], \ldots, x_{p+L-1}[n]]^T$ denote the p-th subarray, we obtain the following form of the estimated covariance matrix:

$$\tilde{\mathbf{R}}[n] = \frac{1}{(M-L+1)N} \sum_{i=n-N}^{n} \sum_{p=1}^{M-L+1} \mathbf{x}_p[i] \mathbf{x}_p^H[i] \tag{2.10}$$

Note that the size of the spatially smoothed $\tilde{\mathbf{R}}[n]$ becomes $L \times L$ and length of the weight vector $\tilde{\mathbf{w}}[n]$ becomes $L \times 1$. Consequently, the output of the spatially smoothed MVDR beamformer is now computed as:

$$y[n] = \frac{1}{(M-L+1)} \sum_{p=1}^{M-L+1} \tilde{\mathbf{w}}^H[n] \mathbf{x}_p^H[n] \tag{2.11}$$

2.3.2 Coherence Factor

The *coherence factor*, or CF, was first proposed by Hollman *et al.* [12] and used to correct the phase distortion due to focusing error. It is defined as the ratio of a coherent sum and an incoherent sum of the input vector elements:

$$\mathrm{CF}[n] = \frac{\left| \sum_{i=1}^{M} x_i[n] \right|^2}{M \sum_{i=1}^{M} \left| x_i^2[n] \right|} \tag{2.12}$$

Park *et al.* [34] applied the CF to the MVDR beamformer as follows:

$$y[n] = \frac{\mathrm{CF}[n]}{(M-L+1)} \sum_{k=1}^{M-L+1} \tilde{\mathbf{w}}^{H}[n]\mathbf{x}_{k}{}^{H}[n] \tag{2.13}$$

which was shown to improve contrast, sidelobe suppression, and resilience against phase distortion. In this thesis, we always multiply our beamformed output by a coherence factor calculated according to Eq. (2.13).

2.3.3 Baseline Simulated Images

Evaluation results in this thesis are based on the simulated 4-MHz ultrasound images of two distinct types: a 12-point phantom acquired by a 98-element phased array and a point-scatterer-cyst phantom acquired by a 192-element linear array with 66 active elements. Our simulations were performed in MATLAB v7.8 using the FIELD-II simulation tool v3.20 [13-15]. In all simulations, we add white Gaussian noise with 60-dB SNR to each sensor signal, and after the beamforming, we compress the signal envelope to the 60-dB dynamic range.

The *12-point phantom* consists of twelve single point targets placed at the 10-mm intervals starting at 30 mm from the transducer surface. Each element of the 98-element phased array has the height of 7 mm, with the inter-element spacing of $\lambda/2$ corresponding to the speed of sound of 1540 m/s. The emitted wave is a Gaussian pulse with the carrier frequency of 4 MHz and the fractional bandwidth (i.e., the ratio of the bandwidth to the carrier frequency) of 70%. During transmission, there is a single fixed focus at 60 mm from the transducer surface, and during reception, dynamic receive focusing is performed at 10-mm intervals. The sampling frequency is set to 100 MHz, and the image consists of 64 scan lines separated by 0.47 degrees. The main motivation of simulating the 12-point phantom is to access the image quality in terms of spatial resolution. The *point-scatterer-cyst phantom* consists of a point target, a highly scattering region with the radius of 1.5

mm, and a water-filled cyst region with the radius of 2 mm. The lateral distances are -14 mm, -5 mm, and 10 mm, respectively. The phantom is placed at 60 mm, which is the transmit focus point. The speckle pattern is simulated with 10 randomly placed scatterers within a resolution cell of λ^3 to ensure fully developed speckle [38]. During reception, dynamic receive focusing is performed at 10-mm intervals. Each element of the 192-element linear array (with 66 active elements) has the height of 5 mm. As with the 12-point phantom, the same sampling frequency and the excitation pulse are used. The resulting 40-mm image consisted of 64 scan lines. The main motivation of simulating the point-scatterer-cyst phantom is to access the image quality in terms of contrast.

Figure 2.1 clearly demonstrates the advantage of MVDR beamforming (with spatial smoothing and without CF scaling of the beamformed output) over rectangular-windowed and Kaiser-windowed DAS beamforming (without CF scaling of the beamformed output) in the case of 12-point phantom. The rectangular-windowed DAS beamformer suffers from high sidelobe levels, which can be improved using the Kaiser window instead. However, the MVDR beamformer yields the highest spatial resolution even beyond the transmit focus point of 60 mm. Figure 2.2 shows that multiplying the output by the CF yields a noticeable improvement in the images produced by DAS and MVDR beamforming (e.g., see points at 110, 120, 130 mm).

Figure 2.3 shows the simulated image of the point-scatterer-cyst phantom. The first two images (corresponding to the rectangular-windowed and Kaiser-windowed DAS beamformers without CF scaling) demonstrate that the water-filled cyst loses its circular shape, and the point is not easily distinguishable from the speckled background. On the other hand, the third image (corresponding to the MVDR beamformer without CF scaling) demonstrates that the water-filled cyst shape is preserved better, and the point is more noticeable due to a reduction in the speckle noise. Applying the coherence factor yields the fourth, fifth and sixth images (corresponding to the rectangular-windowed DAS, Kaiser-windowed DAS, and MVDR beamformers, respectively), demonstrating the more visible point and sharper boundaries of the scatterer and the cyst.

In this thesis, we always multiply the beamformed output by the coherence factor.

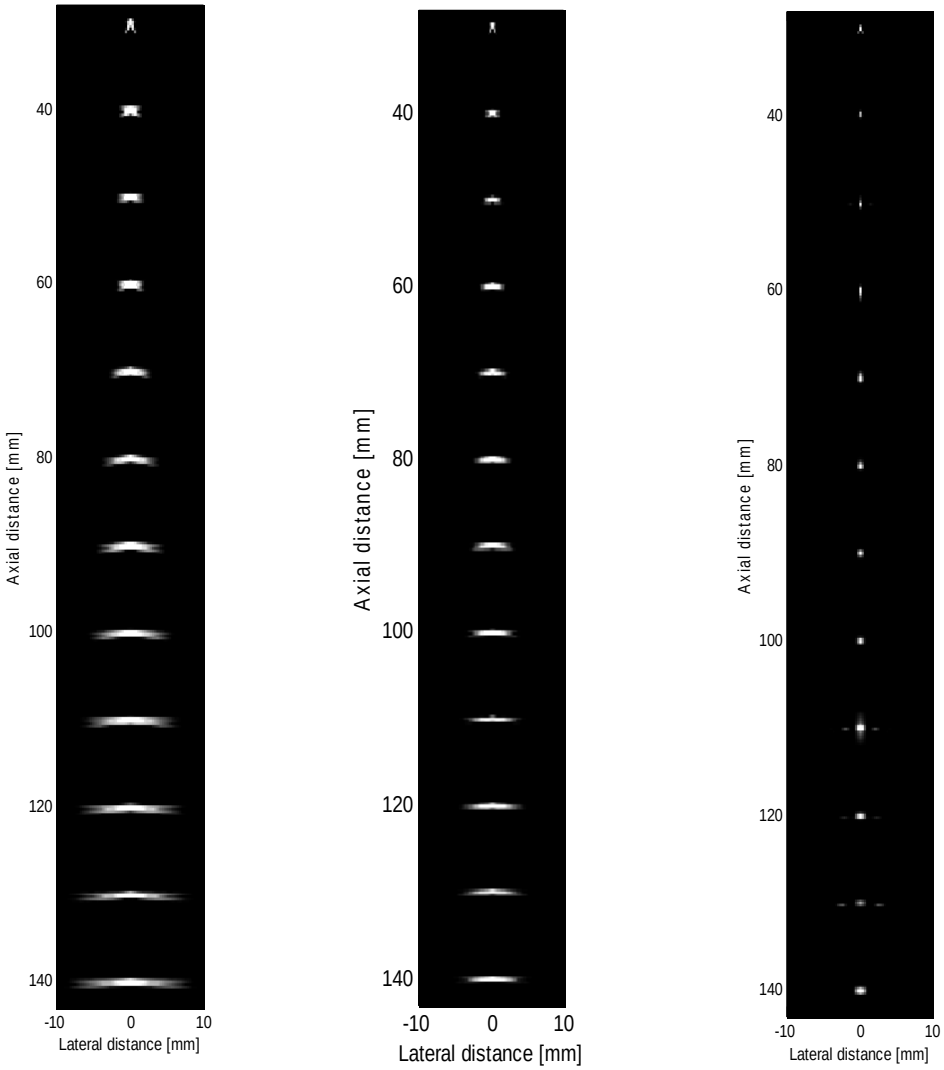

Figure 2.1: Performance of rectangular-windowed DAS (left), Kaiser-windowed DAS (center), and MVDR (right) beamforming without CF scaling: 12-point phantom, point placement in 10-mm intervals, 64 scan lines, 4-MHz 98-element phased array transducer (transmit focus at 60 mm, dynamic receive focus at 10 mm intervals), spatial smoothing with $L = 49$ and $N = 1$.

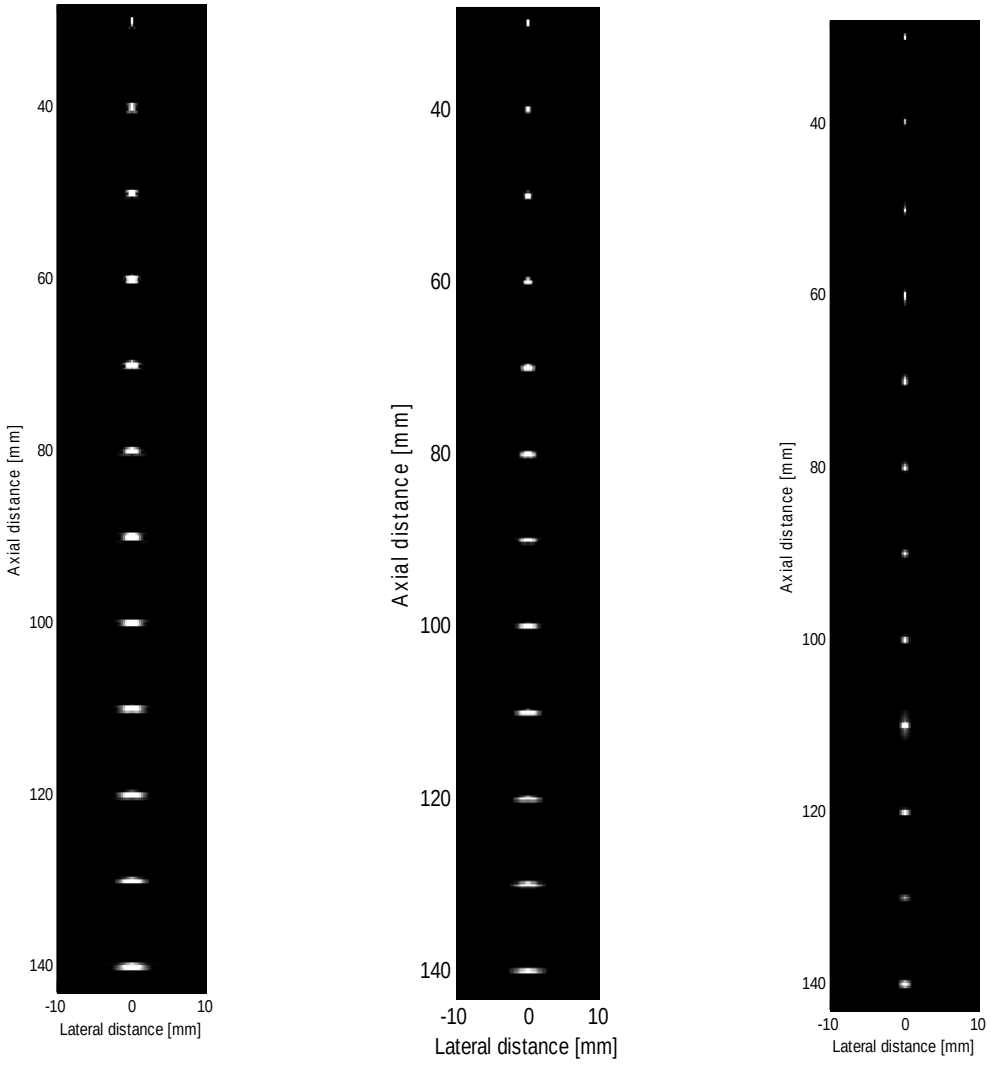

Figure 2.2: Performance of rectangular-windowed DAS (left), Kaiser-windowed DAS (center), and MVDR (right) beamforming with CF scaling: 12-point phantom, point placement in 10-mm intervals, 64 scan lines, 4-MHz 98-element phased array transducer (transmit focus at 60 mm, dynamic receive focus at 10 mm intervals), spatial smoothing with $L = 49$ and $N = 1$.

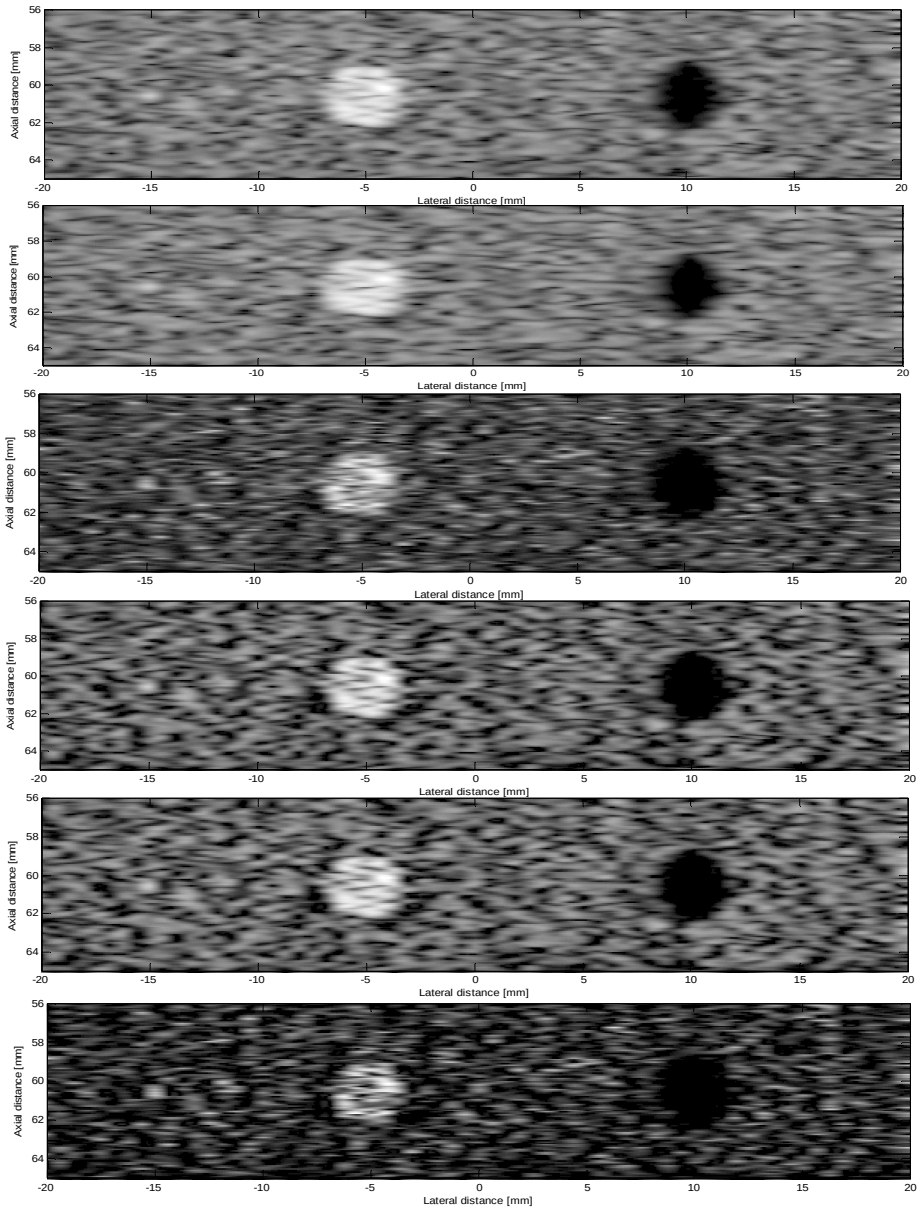

Figure 2.3: From top to bottom: performance of rectangular-windowed DAS, Kaiser-windowed DAS, MVDR (all three without CF scaling), rectangular-windowed DAS, Kaiser-windowed DAS, and MVDR (all three with CF scaling) beamforming: Point-scatterer-cyst phantom placed at 60 mm (lateral placement: single point at −15 mm, 3-mm scattering region at −5 mm, 4-mm water-filled cyst at 10 mm), 64 scan lines, 4-MHz 192-element linear array transducer (66 active elements, transmit focus at 60 mm, dynamic receive focus at 10 mm intervals), spatial smoothing with $L = 33$, using $N = 2$.

2.4 Related Work

Beamforming has been used in many applications, such as radar, sonar, seismology, wireless communications, and medical imaging. Beamforming techniques generally can be classified into two categories: data-independent (non-adaptive) and data-dependent (adaptive) [5, 16, 17]. The weights of the former are fixed and do not depend on the input data; whereas, the weights of the latter vary depending on the statistics of the input data. One of the earliest statistically optimal beamforming methods was the MVDR beamformer due to Capon [18], which is special case of a so-called *linearly constrained minimum variance* (LCMV) beamformer, initially used for narrowband applications. It has been extended to broadband applications in both time-domain and frequency-domain. In the time-domain, the output of each sensor is fed to an FIR filter with several taps, whose weights are chosen to minimize the mean square error of the beamforming output, subject to a set of linear constraints [20]. In the frequency-domain, the signal from each sensor is first transformed into the frequency domain using discrete Fourier transform (DFT), then narrowband beamformers are applied to process the individual frequency bins, and finally the narrowband beamformed outputs are transformed back to the time domain using the inverse discrete Fourier transform (IDFT) [5].

In some applications, where a large number of sensors are available, it is more efficient to perform beamforming in a smaller-dimensional space, which is exemplified by the so-called *beamspace beamformer* and *Generalized Sidelobe Canceller* (GSC) [19]. The former is an example of the deterministic reduction technique: the transformation from the element space to beamspace is accomplished by multiplying the input snapshot by an orthogonal matrix, referred to as the Butler matrix [5]. Each row of the Butler matrix represents a steering vector associated with one orthogonal beam. The selection of the orthogonal beams depends on the prior knowledge of the spatial distribution of the desired signal and the interferers. Alternatively, there are statistical reduction techniques, and they fall into two main categories: the principal component method and the cross-spectral methods. The principal component method, also known as the *eigenbeamformer*,

first reduces the size of the covariance matrix by decomposing it into two orthogonal subspaces, known as the signal plus the interference subspace (represented by the largest eigenvalues and their associated eigenvectors) and the noise subspace (represented by the smallest eigenvalues and their associated eigenvectors), and then performs beamforming in the signal plus the interference subspace [5]. The cross-spectral method, on the other hand, is commonly realized by the GSC structure, where the selection of the reduced subspace is driven by retaining the eigenvectors that maximize the signal to interference plus noise ratio SINR [21].

Over the past years, the ultrasound imaging literature has been growing with reports on the application of various beamforming methods, including both non-adaptive [22-28] and adaptive. In this thesis we focus on adaptive beamforming, briefly reviewed next.

Sasso and Cohen-Barcie [10] were among the first to apply the spatially smoothed MVDR beamformer to ultrasound imaging, which demonstrated an improvement in the target resolution and contrast. To increase the robustness of the MVDR beamformer against the error between the actual and the presumed sound speed, Wang et *al*. [29] used a synthetic aperture, in which the medium was insonified by multiple beams from different spatial positions to obtain a robust covariance matrix. In such an aperture, each beam was generated by a single transmitting element, and the echoes were received by the entire array, i.e., each point in the image had as many observations as the number of the transmitting elements. A similar approach (combined with spatial smoothing) was investigated by Vigonon and Burcher [30], except they used 16 focused beams as opposed to 32, 64, 128 divergent beams used in [29]. Both methods were tested on simulated and experimental data, demonstrating high resolution and contrast compared with the DAS beamformer. Synnevag *et al.* [31] increased the robustness of the MVDR beamformer by means of diagonal loading of the estimated covariance matrix (together with spatial smoothing), demonstrating reduced sensitivity of the MVDR beamformer to the sound speed variations at the expense of the reduced lateral resolution. Asl and Mahloojifar [32] applied the eigenbeamformer to medical ultrasound. They projected the MVDR weight vector onto the signal subspace of the covariance matrix and demonstrated (through simulations of point targets and cyst phantom) an increase in

contrast and robustness against overestimation of the speed of sound. The same authors in [33] forward-backward spatial averaging of the estimated covariance matrix, which resulted in an increase in contrast without sacrificing resolution at the presence of sound speed errors. The coherence factor was first applied to ultrasound imaging by Hollman *et al* [12], and it has been used by many researchers to scale the output of both non-adaptive and adaptive beamforming [34-36]. Nilson and Holm [36] showed that multiplying the output of the DAS beamformer by the CF can be interpreted as processing the output of the DAS beamformer using the Wiener postfilter. Likewise, multiplying the output of the MVDR beamformer is equivalent to using the Wiener beamformer [5].

The abovementioned references focused with adaptive narrowband beamforming. Since ultrasound is broadband in nature, several researchers have investigated broadband beamforming in the context of ultrasound imaging. Mann and Walker [37] studied the performance of the time-domain Frost beamformer using multiple linear constraints. The order of each FIR filter was set to 10, the number of sensors was 128, and a diagonal loading was used to ensure a well-conditioned covariance matrix estimate. The resulting images of a single point target and a cyst phantom showed a 2x improvement in the point target resolution and 60% improvement in the cyst contrast. Holfort *et al.* [38] applied broadband beamforming in the frequency-domain to simulated point targets and a cyst phantom. In their study, the spatially smoothed data was transformed to the frequency-domain using short time Fourier transform, and then each individual subband data was beamformed using MVDR the beamformer. The results were compared with the DAS and Hanning beamformers, which demonstrated significant improvements in both the resolution and contrast. Viola and Walker in [39] studied four adaptive beamformers from [11, 20, 41, 42], applied to two different types of phantoms: wire targets and a cyst phantom. Their simulations showed that the adaptive beamformers from [11, 20, 41, 42] achieved higher resolution in comparison to the DAS beamformer. They also observed that the three beamformers from [11, 41, 42] significantly reduced the sidelobe levels. The beamformer from [41] was superior with sidelobe levels of roughly -110 dB, which

is practically at the noise level. Motivated the superior performance of the beamformer in [41], the same authors proposed its broadband extension in [40], called Time-domain, Optimized, Near-field Estimator (TONE). Their idea was based on a linear model of the image formation, where the region of interest is subdivided into a collection of hypothetical targets at arbitrary positions in a sampling grid. For each hypothetical target in the region of interest the spatial response is computed experimentally, theoretically, or using simulation. Based on the computed spatial response and the received data, the distribution and the intensity of the matching hypothetical targets were found using the maximum a posteriori (MAP) estimation technique. Although this beamformer offers excellent broadband performance, its high computational complexity may prohibit its use in practice.

Several researchers have attempted to reduce the computational complexity of the adaptive beamforming. Synnevag *et al*. [28] have proposed a beamformer that uses several predefined windows that satisfy the distortionless constraint and selects the one that reduces the output power. Khezerloo and Rakhmatov [50] have proposed gradient-driven and reduced-rate GSC-based beamforming that uses an approximate covariance matrix inverse obtained using a conjugate gradient algorithm with only three iterations. Nilsen and Hafizovic [43] have implemented the Capon beamformer in the beam-space (rather than in the element-space) assuming a priori knowledge of the distribution of the desired signal. They have used three beams with the greatest energy footprint, which resulted in the image quality comparable to that of the Capon beamformer. Finally, Hall *et al*. [51] have proposed a method that suppresses the DAS beamformed snapshot, if the corresponding CF value is below some threshold value.

2.5 Our Contribution

As we have mentioned in Chapter 1, the main objective of our work has been to reduce the computational load of adaptive beamforming without significant degradation

in the ultrasound image quality. Our simple approach is based on switching between a non-adaptive beamformer and an adaptive one based on the CF value. For each input vector, we calculate the corresponding CF and compare it to a certain threshold T_{CF}. If CF < T_{CF}, we use non-adaptive DAS beamforming; otherwise, we use adaptive MVDR beamforming implemented by the *Generalized Sidelobe Canceller* (GSC) presented in Chapter 3. The main difference between our scheme and that from [51] is in the usage of the adaptive versus non-adaptive beamformers: we do not suppress the DAS beamformer output based on the threshold as it is done in [51]; instead, we simply switch between adaptive beamforming and non-adaptive beamforming. In addition to evaluating GSC-based beamforming, we also investigate the performance of the so-called *Adaptive Single Snapshot Beamformer* (ASSB) presented in Chapter 4. The application of the ASSB to ultrasound was first mentioned in [39] very briefly, providing a somewhat cursory treatment without addressing any computational complexity issues.

As discussed in Chapter 5, our hybrid scheme turns out to be highly effective despite its simplicity, yielding significant computational savings (between 59% and 99%) without significant degradation in the image quality (less than 5% in terms of resolution and contrast). To re-iterate, this thesis makes the following contributions that have been overlooked in the existing literature on ultrasound imaging:

- We apply the *hybrid GSC-based beamforming* method to ultrasound imaging and evaluate its performance using several switching thresholds associated with the coherence factor of the received input vectors.
- We apply the *hybrid ASSB-based beamforming* method to ultrasound imaging and evaluate its performance using several switching thresholds associated with the coherence factor of the received input vectors.
- We estimate and quantitatively compare the computational costs of the hybrid GSC-based and ASSB-based beamformers to those of their always-adaptive counterparts, thus exposing the *quality-cost tradeoffs* that are enabled by hybrid beamforming.

Chapter 3

Hybrid GSC-based Beamforming

In this chapter we discuss the underlying theory of the *generalized sidelobe canceller* (GSC) beamformer and its computational complexity. We also propose a simple yet effective technique for reducing the computational cost of beamforming by switching between adaptive GSC-based and nonadaptive DAS-based weight calculations. We perform such switching based on the value of the coherence factor compared to a certain threshold.

3.1 GSC Beamforming

The MVDR beamformer can be implemented by an equivalent structure shown in Figure 3.1 and known as the GSC beamformer. The upper path with the nonadaptive weight vector $\mathbf{w}_q$ satisfies the look direction constraint and is referred to as quiescent response. The term "quiescent response" means that in a quiet environment (i.e., in the absence of any interferers) the upper path provides an optimal set of weights. It is implemented using the DAS beamformer with L fixed weights, i.e., $\mathbf{w}_q = \frac{\mathbf{1}}{L}$.

The lower path is referred to as the sidelobe cancelling branch, where the application of the adaptive weight vector $\mathbf{w}_a$ is preceded by preprocessing that uses a blocking matrix

B of size $L\times(L-1)$. The blocking matrix ensures that only signals coming from the non-look direction are admitted. It also reduces the $L\times L$ spatially smoothed sample covariance matrix $\tilde{\mathbf{R}}[n]$ to the smaller $(L-1)\times(L-1)$ covariance matrix $\mathbf{R}_z[n]=\mathbf{B}^H\tilde{\mathbf{R}}[n]\mathbf{B}$.

The GSC beamformer equation can be written as follows:

$$y[n]=\frac{1}{M-L+1}\sum_{p=1}^{M-L+1}\mathbf{w}[n]^H\mathbf{x}_p[n]$$

$$\mathbf{w}[n]=\mathbf{w}_q-\mathbf{B}^H\mathbf{w}_a[n] \tag{3.1}$$

$$\mathbf{w}_a[n]=\left(\mathbf{B}^H\tilde{\mathbf{R}}[n]\mathbf{B}\right)^{-1}\mathbf{B}^H\tilde{\mathbf{R}}[n]\mathbf{w}_q=\mathbf{R}_z^{-1}[n]\mathbf{p}_z[n] \tag{3.2}$$

where

$$\mathbf{x}_p[n]=[x_p[n],x_{p+1}[n],...,x_{p+L-1}[n]]^T$$

$$\mathbf{p}_z[n]=\mathbf{B}^H\tilde{\mathbf{R}}[n]\mathbf{w}_q.$$

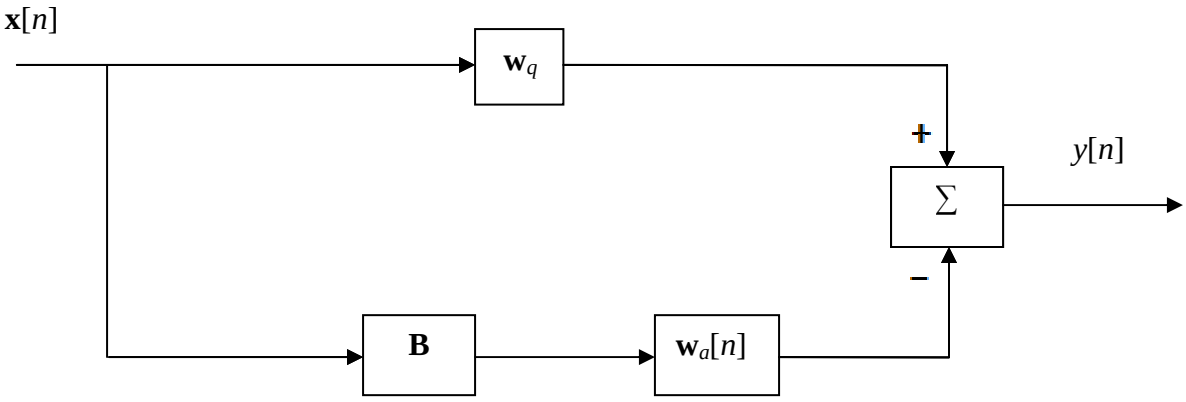

Figure 3.1: Generalized sidelobe canceller.

Recall that the blocking matrix $\mathbf{B}$ must prevent the signals coming from the desired direction from leaking into the lower path. In other words, the block matrix must satisfy:

$$\mathbf{B}^H \mathbf{w}_q = \mathbf{0} \tag{3.3}$$

In order to satisfy the above condition the columns of $\mathbf{B}$ must be linearly independent and sum up to zero. One such matrix **B** is suggested in [19] and shown below. We prefer this type of blocking matrix, due to its sparse structure that reduces the computational complexity.

$$\mathbf{B} = \begin{bmatrix} 1 & 0 & \cdots & 0 & 0 \\ -1 & 1 & \vdots & \vdots & \vdots \\ 0 & -1 & \ddots & 0 & 0 \\ 0 & 0 & \ddots & 1 & 0 \\ \vdots & \vdots & \vdots & -1 & 1 \\ 0 & 0 & \cdots & 0 & -1 \end{bmatrix}$$

3.2 Proposed Method

In Chapter 2 we have demonstrated that using the adaptive MVDR beamformer over the nonadaptive DAS beamformer significantly improves the ultrasound image quality. Also, recall that the output $y[n]$ of both beamformers was multiplied by the coherence factor CF[n] taking the values between 0 and 1. When the array is steered towards the broadside direction (i.e., to make the incidence angle equal to $\frac{\pi}{2}$), the steering vector becomes:

$$\mathbf{a} = \begin{bmatrix} 1 \\ 1 \\ : \\ : \\ 1 \end{bmatrix} \tag{3.4}$$

Therefore,

$$\mathrm{CF}[n] = \frac{\left|\mathbf{a}^H \mathbf{x}\right|^2}{M\sum_{i=1}^{M}\left|x_i^2[n]\right|} = \frac{\left|\sum_{i=1}^{M} x_i[n]\right|^2}{M\sum_{i=1}^{M}\left|x_i^2[n]\right|} \tag{3.5}$$

Equation (3.5) can be understood as the ratio of the on-axis power to the total received power, which gives us some insight into the characteristics of the received signals. High CF values indicate that the most of the received energy is in the mainlobe region. In such situations, we need to use the adaptive MVDR beamformer to null the interferers and extract the desired signal with the unity gain. On the other hand, low CF values indicate that the most of the received energy is in the sidelobes. In such situations we can employ nonadaptive DAS-based beamforming without significantly worsening the image quality. In other words, we propose to use the CF value for a given input vector $\mathbf{x}[n]$ to make a decision on the use of adaptive versus nonadaptive beamforming. Since the nonadaptive DAS beamformer has a significantly lower computational cost than that of the adaptive MVDR beamformer (involving matrix inversions), our approach gives rise to significant computational savings, as demonstrated in Chapter 5.

Given a GSC realization of the MVDR beamformer and an appropriate threshold value, denoted by T_{CF}, our proposed method can be summarized as follows:

1. Given input vector $\mathbf{x}[n]$, compute $\mathrm{CF}[n]$.
2. If $\mathrm{CF}[n] \geq T_{CF}$, then use the GSC beamformer to calculate output $y[n]$, else use the DAS beamformer to calculate output $y[n]$.
3. Let $y[n] \leftarrow y[n] \cdot \mathrm{CF}[n]$.

3.3 Computational Complexity Analysis

To evaluate the amount of the computational savings due to the use of our method (in comparison to always-adaptive beamforming), let V denote the total number of input vectors processed to form an ultrasound image, and let V_{GSC} denote the number of input vectors processed adaptively, i.e., the number of input vectors $\mathbf{x}[n]$ satisfying the condition $\mathrm{CF}[n] \geq T_{CF}$. Then, the cost of our method equals $V_{GSC} \cdot Cost(\mathrm{GSC}) + (V - V_{GSC}) \cdot Cost(\mathrm{DAS})$, as opposed to the always-adaptive beamforming cost of $V \cdot Cost(\mathrm{GSC})$. Hence, the resulting computational savings are as follows:

$$\begin{aligned} Savings &= \frac{V \cdot Cost(GSC) - V_{GSC} \cdot Cost(GSC) - (V - V_{GSC}) \cdot Cost(DAS)}{V \cdot Cost(GSC)} \times 100\% \\ &= \left(1 - \frac{V_{GSC}}{V}\right)\left(1 - \frac{Cost(DAS)}{Cost(GSC)}\right) \times 100\%. \end{aligned} \tag{3.6}$$

Note that the factor $(1 - V_{GSC}/V)$ depends on both the choice of the CF threshold value T_{CF} and the processed input vectors, while the factor $(1 - Cost(\mathrm{DAS})/Cost(\mathrm{GSC}))$ is threshold-independent and data-independent. Next, we present the cost analysis for the DAS and GSC beamformers and analyse the corresponding cost ratio.

Let a, m, and r denote the computational costs of a single addition, multiplication, and square-root operation, respectively. We also assume that the cost of a division operation is m as well. Given the input vector $\mathbf{x}[n]$ of size M, the cost of calculating $\mathrm{CF}[n]$ is $2(M-1)a + (M+3)m$, and the cost of calculating the DAS output $y[n]$ is $(M-1)a + m$ (including one multiplication by $\mathrm{CF}[n]$). However, when computing $y[n]$, we can reuse the intermediate result $\frac{\sum_{i=1}^{M} x_i}{M}$ computed for $\mathrm{CF}[n]$, i.e., we only need a multiplication by $\mathrm{CF}[n]$. Thus,

$$Cost(\mathrm{DAS}) = 2(M-1)a + (M+3)m + m = 2(M-1)a + (M+4)m. \tag{3.7}$$

On the other hand, the cost of calculating the GSC output $y[n]$ for a single snapshot is dominated by the cost of inverting matrix $\mathbf{R_z}[n]$ and involves $O(L^3)$ additions, $O(L^3)$ multiplications, $O(L)$ square-roots, and $O(1)$ divisions. Following [44] and [45], Table 3.1 provides a breakdown of computational costs associated with the GSC-based beamformer:

$$\begin{aligned} Cost(\text{GSC}) = & \left(\frac{L^3}{6}+\frac{5L^2}{2}+2M(L+1)-\frac{23L}{3}+1\right)a + \\ & \left(\frac{L^3}{6}+L^2+M(L+1)-\frac{7L}{6}+5\right)m + \\ & (L-1)r\,. \end{aligned} \tag{3.8}$$

Since $L \le M/2$, then the ratio $\frac{Cost(DAS)}{Cost(GSC)}$ is bounded by $O(M^2)$.

Table 3.1: Computational cost of each GSC-based beamforming step [44, 45].

Steps needed to calculate the output of GSC		Addition	Multiplication	Square Root
$\tilde{\mathbf{R}}[n]$	$N = 1$	$L(M-1)$	$L(M+1)$	0
	$N = 2$	$L(M-1)+L(L+1)/2$	$L(M+1)$	
$\mathbf{D}=\mathbf{B}^H\mathbf{R}[n]$		$L(L-1)$	0	0
$\mathbf{R}_z[n]=\mathbf{DB}$		$(L-1)^2$	0	0
$\mathbf{p}_z=\mathbf{D}\mathbf{w}_q$		$(L-1)^2$	$(L-1)$	0
$\mathbf{R}_z[n]=\mathbf{G}\mathbf{G}^H$		$\frac{L^3}{6}-\frac{L^2}{2}+\frac{L}{3}$	$\frac{L^3}{6}-\frac{5L}{6}+1$	$L-1$
$\mathbf{G}\mathbf{G}^H\mathbf{w}_a=\mathbf{p}_z$		L^2-3L+2	L^2-L	0
$y[n]$ Output of GSC		$ML-L^2+L-1$	$L+1$	0
$y[n]$ Total output of GSC plus CF	$N = 1$	$\frac{L^3}{6}+\frac{5L^2}{2}+2M(L+1)-\frac{23L}{3}+1$	$\frac{L^3}{6}+L^2+M(L+1)-\frac{7L}{6}+5$	$L-1$
	$N = 2$	$\frac{L^3}{6}+3L^2+2M(L+1)-\frac{43L}{6}+1$		
$y[n]$ Output of DAS plus CF		$2(M-1)$	$M+4$	0

Chapter 4

Hybrid ASSB-based Beamforming

This chapter introduces the so-called *adaptive single snapshot beamformer* and discusses its suitability for ultrasound imaging. The adaptive single snapshot beamformer is known to reject nonstationary and coherent interferers. This important feature is particularly relevant to ultrasound data, and it offers an interesting alternative to the GSC beamformer with spatial smoothing.

4.1 Introduction

We assume that there are *K* signals recorded by the *M* receiving sensors, as shown in Figure 4.1. One of the incident signals is the desired signal and denoted by $s_1[n]$, and the rest are the unwanted or interfering signals denoted by $s_2[n], s_3[n], ..., s_K[n]$. In a noisy environment, we can represent the incident signal at the n-th snapshot as:

$$\mathbf{x}[n] = \sum_{i=1}^{K} \mathbf{e}(\theta_i) s_i[n] + \mathbf{n}[n] \tag{4.1}$$

where

θ_i is the incidence angle of the wave s_i,

$\mathbf{e}(\theta_i)$ is the steering vector associated with the i-th signal and is written as

$$\mathbf{e}(\theta_i) = [1, e^{-j\frac{2\pi}{\lambda}d\sin(\theta_i)}, ..., e^{-j\frac{2\pi}{\lambda}(M-1)d\sin(\theta_i)}]^H ,$$

d is the spacing between adjacent elements,

$\mathbf{n}[n]$ is the additive white noise vector at the n-th snapshot.

To further simplify the notations, we write equation (4.1) as:

$$\mathbf{x}[n] = \mathbf{E}\mathbf{s}[n] + \mathbf{n}[n] \tag{4.2}$$

where $\mathbf{s}[n] = [s_1[n], ..., s_K[n]]^T$, and $\mathbf{E} = [\mathbf{e}(\theta_1), ..., \mathbf{e}(\theta_K)]$ is the $M \times K$ matrix. Then, the covariance matrix of the n-th snapshot is

$$\mathbf{R}[n] = E\{\mathbf{x}[n]\mathbf{x}^H[n]\} = \mathbf{E}\mathbf{S}\mathbf{E}^H + \sigma^2\mathbf{I} , \tag{4.3}$$

where

$\mathbf{S}[n] = E\{\mathbf{s}[n]\mathbf{s}^H[n]\}$, and σ^2 is the average power of the noise.

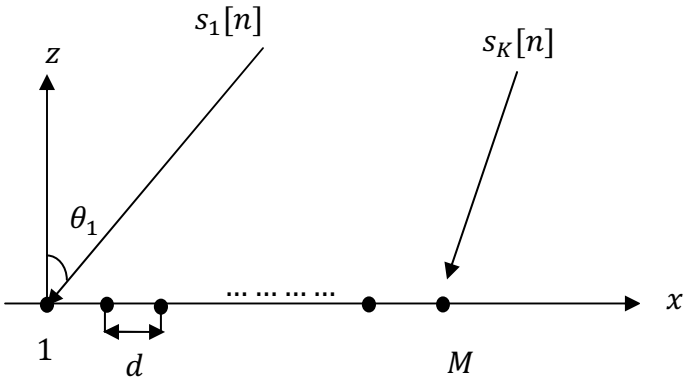

Figure 4.1: K source signals incident on uniform linear array M sensors.

When the input signals are not correlated, the matrix $\mathbf{S}[n]$ is diagonal and invertible. On the other hand, if the signals are correlated or coherent, then the matrix $\mathbf{S}[n]$ becomes

non-diagonal and noninvertible, and one must use, for example, spatial smoothing technique [46] in order to decorrelate the on-axis and off-axis signals and restore the rank of the matrix $\mathbf{S}[n]$. Alternatively, Markus and Schreib [42] proposed a method that not only handles the existence of coherent signals, but also works in a nonstationary environment. It is called adaptive single snapshot beamforming, which is described next, according to [42].

4.2 Adaptive Single Snapshot Beamformer

The adaptive single snapshot beamformer (ASSB) can be considered as a deterministic beamforming technique because it does not make any use of the statistics of the input snapshot. The basic idea of the ASSB is first to divide the *M*-sensor array into P overlapping groups with each group having L elements, as shown in Figure 4.2. It is assumed that the following relation is satisfied:

$$P \geq L \geq K \tag{4.4}$$

Hence, for every incident signal $s_i[n]$ with an incident angle $\theta_i[n]$, there are two manifold vectors associated with it. The first one is denoted by $\mathbf{g}_i[\theta_i]$ and called the *group characteristic vector* of size L (related to L sensors in each group), and the second one is denoted by $\mathbf{a}_i[\theta_i]$ and called the *array characteristic vector* of size P (related to P groups in the array). Next we define our noise-free *single-snapshot data matrix* as:

$$\mathbf{X} = \mathbf{A}\cdot\text{diag}(s_1, s_2, \ldots, s_K)\cdot\mathbf{G}^T \tag{4.5}$$

where

$$\mathbf{A} = [\mathbf{a}_1, \mathbf{a}_2, \ldots, \mathbf{a}_K]$$

$$\mathbf{G}^T = \text{col}[\mathbf{g}_1{}^T, \mathbf{g}_2{}^T, \ldots, \mathbf{g}_K{}^T].$$

Equivalently, equation can be written as:

$$\mathbf{X} = \sum_{i=1}^{K} \begin{bmatrix} a_1(\theta_i)\mathbf{g}_i{}^T(\theta_i) \\ \cdot \\ \cdot \\ a_P(\theta_i)\mathbf{g}_i{}^T(\theta_i) \end{bmatrix} \cdot s_i = \sum_{i=1}^{K} \mathbf{a}_i \mathbf{g}_i{}^T \cdot s_i \tag{4.6}$$

To illustrate the ASSB operation in the noise-free case, we let $s_1[n]$ represent our desired signal and assume that (after steering toward the broadside) the corresponding P-element vector $\mathbf{a}_1 = [1, 1, \ldots, 1]^T$ and L-element vector $\mathbf{g}_1 = [1, 1, \ldots, 1]^T$. Then, according to [42], we can express the ASSB output $y[n] \approx s_1[n]$ using the following bilinear form:

$$y = \mathbf{u}^T \mathbf{X} \mathbf{v}, \tag{4.7}$$

where $\mathbf{v}[n]$ is called the *group weight vector*, and $\mathbf{u}[n]$ is called the *array weight vector* (see Figure 4.1).

Given such a formulation, the beamforming problem can be interpreted as finding scalar y that reduces the rank of $\mathbf{X} - (\mathbf{a}_1\mathbf{g}_1{}^T)y$, which corresponds to the following generalized eigenvalue problems [42]:

$$(\mathbf{X} - (\mathbf{a}_1\mathbf{g}_1{}^T)y)\mathbf{v} = \mathbf{0} \tag{4.8}$$

$$\mathbf{u}^T(\mathbf{X} - (\mathbf{a}_1\mathbf{g}_1{}^T)y) = \mathbf{0}^T \tag{4.9}$$

In order to pass the desired signal undistorted, a unity gain constraint must be imposed, leading to the following problem re-formulation:

$$(\mathbf{X} - (\mathbf{a}_1\mathbf{g}_1{}^T)y)\mathbf{v} = \mathbf{0}, \text{ subject to } \mathbf{g}_1{}^T\mathbf{v} = 1, \tag{4.10}$$

or

$$\begin{bmatrix} \mathbf{g}_1^{\,T} & 0 \\ \mathbf{X} & -\mathbf{a}_1 \end{bmatrix} \begin{bmatrix} \mathbf{v} \\ y \end{bmatrix} = \begin{bmatrix} 1 \\ \mathbf{0} \end{bmatrix}. \tag{4.11}$$

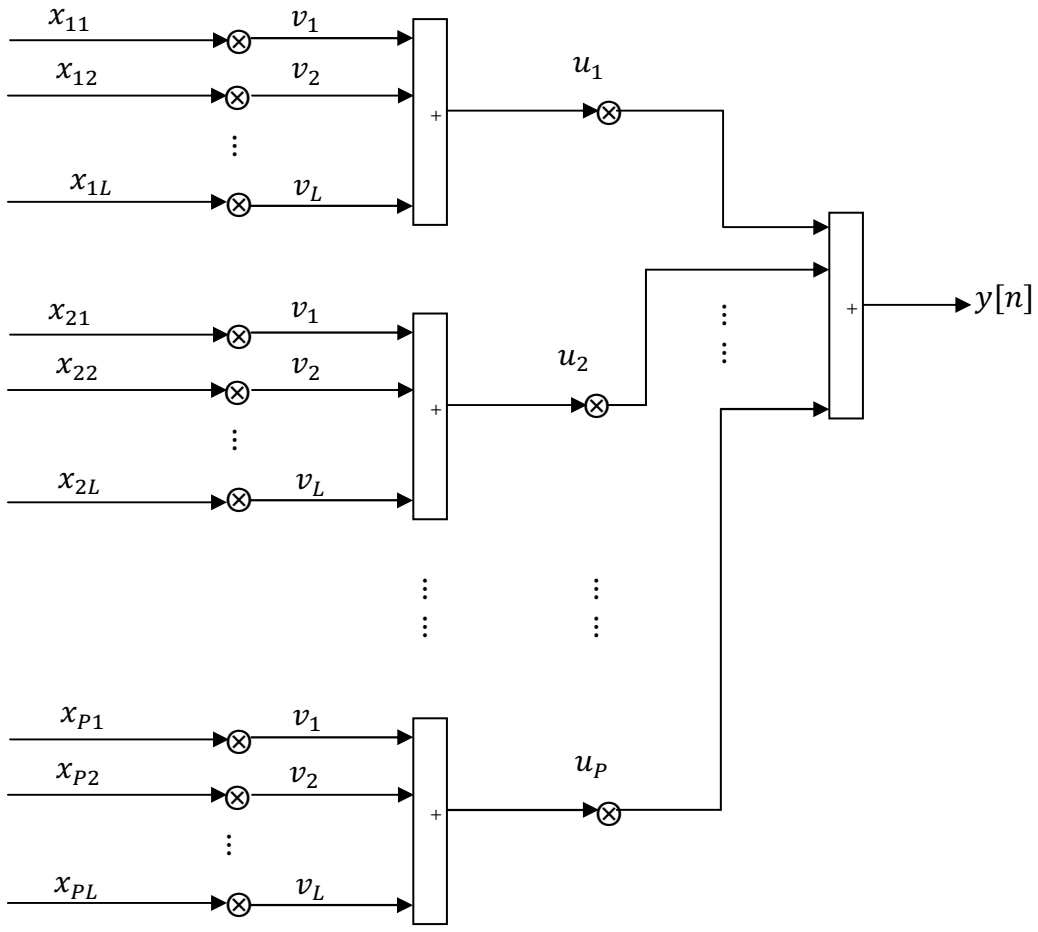

Figure 4.2: Adaptive single snapshot beamformer structure [42].

Letting $\mathbf{A} = \begin{bmatrix} \mathbf{g}_1^{\,T} & 0 \\ \mathbf{X} & -\mathbf{a}_1 \end{bmatrix}$, $\mathbf{b} = [1, \mathbf{0}]^T$, and $\mathbf{z} = [\mathbf{v}, y]^T$, we obtain $\mathbf{z} = \mathbf{A}^{-1}\mathbf{b}$, where the desired signal y is the last element of the vector $\mathbf{z}$.

In the presence of noise, we let our data matrix be

$$\tilde{\mathbf{X}} = \mathbf{X} + \mathbf{N} \tag{4.12}$$

where $\mathbf{N}$ is the $P \times L$ noise matrix corresponding to the $P \times L$ sensors and defined as

$$\mathbf{N} = \begin{bmatrix} \mathbf{n}_1^T \\ \mathbf{n}_2^T \\ \vdots \\ \mathbf{n}_P^T \end{bmatrix},$$

where $\mathbf{n}_j$ represents a noise vector at the j-th group of L sensors of the P-group array.

Then, our beamforming problem can be approximated as follows [42]:

$$\min_{\mathbf{v},y} \|\mathbf{e}\|_2^2 \quad \text{subject to} \quad \begin{bmatrix} \mathbf{g}_1^T & 0 \\ \tilde{\mathbf{X}} & -\mathbf{a}_1 \end{bmatrix} \begin{bmatrix} \mathbf{v} \\ y \end{bmatrix} = \begin{bmatrix} 1 \\ \mathbf{e} \end{bmatrix}, \tag{4.13}$$

which essentially is a perturbed version of (4.10).

4.3 Proposed Method

The optimization problem given by (4.13) can be solved by standard linear-algebra algorithms that convert the constrained problem into a nonconstrained one using the basis of the null space [42, 47]. Alternatively, we employ a more efficient method that utilizes Lagrange multipliers [48] and takes advantage of the fact that and $\mathbf{g}_1^T \mathbf{v} = 1$.

We have:

$$\mathbf{e} = \mathbf{X}\mathbf{v} - \mathbf{a}_1 y = \begin{bmatrix} \mathbf{X} & \vdots & -\mathbf{a}_1 \end{bmatrix} \begin{bmatrix} \mathbf{v} \\ \cdots \\ y \end{bmatrix} = \mathbf{A}\mathbf{x}_{ls} \tag{4.14}$$

$$\mathbf{g}_1{}^T\mathbf{v} = \begin{bmatrix}\mathbf{g}_1{}^T & \vdots & 0\end{bmatrix}\begin{bmatrix}\mathbf{v}\\ \cdots \\ y\end{bmatrix} = \mathbf{b}^H\mathbf{x}_{ls} = 1 \tag{4.15}$$

Hence, using our new variables **A**, **b**, and $\mathbf{x}_{ls}$, we can re-formulate the problem given by (4.13) as follows:

$$\min \left\|\mathbf{A}\mathbf{x}_{ls}\right\|_2^2, \text{ subject to } \mathbf{b}^H\mathbf{x}_{ls} = 1. \tag{4.16}$$

The problem above can be solved by using Lagrange multipliers:

$$J(\mathbf{x}_{ls};\lambda) = \mathbf{x}_{ls}^H\mathbf{A}^H\mathbf{A}\mathbf{x}_{ls} + \lambda(\mathbf{x}_{ls}^T\mathbf{b} - 1) \ . \tag{4.17}$$

Taking the gradient with respect to $\mathbf{x}_{ls}^H$ and solving for $\mathbf{x}_{ls}$ we obtain

$$\frac{\partial J(\mathbf{x}_{ls};\lambda)}{\partial \mathbf{x}_{ls}} = 2\mathbf{A}^H\mathbf{A}\mathbf{x}_{ls} + \lambda\mathbf{b} = \mathbf{0}, \tag{4.18}$$

$$\mathbf{x}_{ls} = \frac{-\lambda(\mathbf{A}^H\mathbf{A})^{-1}\mathbf{b}}{2}. \tag{4.19}$$

By substituting (4.19) into the constraint equation, the value of λ is given by:

$$\lambda = -(\mathbf{b}^H(\mathbf{A}^H\mathbf{A})^{-1}\mathbf{b})^{-1}. \tag{4.20}$$

Substituting equation (4.20) into (4.19) yields

$$\mathbf{x}_{ls} = \frac{(\mathbf{A}^H\mathbf{A})^{-1}\mathbf{b}}{\mathbf{b}^H(\mathbf{A}^H\mathbf{A})^{-1}\mathbf{b}} = \frac{\mathbf{A}_s^{-1}\mathbf{b}}{\mathbf{b}^H\mathbf{A}_s^{-1}\mathbf{b}}. \tag{4.21}$$

We now recall that the desired signal *y* is the last element of $\mathbf{x}_{ls}$. Therefore, there is no need to solve for the vector $\mathbf{u}^T$. Nevertheless, it is shown in [42] that

$$\mathbf{u}^T = \frac{\mathbf{a}_1}{\|\mathbf{a}_1\|_2^2}. \tag{4.22}$$

Equation (4.22) can be proven as follows. In any least squares problem [49], the residual vector $\mathbf{e}$ is orthogonal to the column space of the data matrix $\tilde{\mathbf{X}}$. Also, when converting the constrained least squares problem in equation (4.13), note that the vector $\mathbf{a}_1$ becomes a column of the data matrix $\tilde{\mathbf{X}}$, that means the residual vector $\mathbf{e}$ is orthogonal to the vector $\mathbf{a}_1$. Based on this fact and the equation (4.13), we can write

$$\mathbf{a}_1 y = \mathbf{X}\mathbf{v} - \mathbf{e} \tag{4.23}$$

Upon post-multiplying both sides by $\frac{\mathbf{a}_1^H}{\|\mathbf{a}_1\|_2^2}$, we obtain

$$\frac{\mathbf{a}_1^H}{\|\mathbf{a}_1\|_2^2}\mathbf{a}_1 y = \frac{\mathbf{a}_1^H}{\|\mathbf{a}_1\|_2^2}\mathbf{X}\mathbf{v} - \frac{\mathbf{a}_1^H}{\|\mathbf{a}_1\|_2^2}\mathbf{e} \tag{4.24}$$

Since $\mathbf{a}_1$ and $\mathbf{e}$ are orthogonal to each other, their inner product is zero, and we have:

$$y = \frac{\mathbf{a}_1^H}{\|\mathbf{a}_1\|_2^2}\mathbf{X}\mathbf{v} \tag{4.25}$$

Comparing equations (4.24) and (4.7), one can see that

$$\mathbf{u}^T = \frac{\mathbf{a}_1^H}{\|\mathbf{a}_1\|_2^2} = \frac{\mathbf{a}_1^H}{P} \tag{4.26}$$

Note that the array weight vector $\mathbf{u}^T$ corresponds to delay-and-sum beamforming of outputs of P groups of the sensor array, where each L-element group is beamformed using the group weight vector v acting on **X**.

4.5 Computational Complexity Analysis

Table 4.1 provides an insight into the amount of computations that are performed by eth ASSB at each beamforming step. Matrix inversion calculations (based on the Cholesky decomposition and forward-backward substitution) are a dominant contributor to the cost. Similar to the hybrid GSC-based beamfomer, we reduce the computational complexity by using the hybrid ASSB-based beamformer that switches between DAS and ASSB beamforming based on the CF values in relation to the threshold T_{CF}.

Let V denote the total number of input vectors processed to form an ultrasound image, and let V_{ASSB} denote the number of input vectors processed adaptively, i.e., the number of input vectors $\mathbf{x}[n]$ satisfying the condition $\mathrm{CF}[n] \geq T_{CF}$. Then, the cost of our method equals $V_{ASSB} \cdot Cost(\mathrm{ASSB}) + (V - V_{ASSB}) \cdot Cost(\mathrm{DAS})$, as opposed to the always-adaptive beamforming cost of $V \cdot Cost(\mathrm{ASSB})$. Hence, the resulting computational savings are as follows:

$$\begin{aligned} Savings &= \frac{V \cdot Cost(\mathrm{ASSB}) - V_{ASSB} \cdot Cost(ASSB) - (V - V_{ASSB}) \cdot Cost(DAS)}{V \cdot Cost(ASSB)} \times 100\% \\ &= \left(1 - \frac{V_{ASSB}}{V}\right)\left(1 - \frac{Cost(DAS)}{Cost(ASSB)}\right) \times 100\%. \end{aligned} \tag{4.27}$$

Note that the factor $(1 - V_{ASSB}/V)$ depends on both the choice of T_{CF} and the processed input vectors, while the factor $(1 - Cost(\mathrm{DAS})/Cost(\mathrm{ASSB}))$ is threshold-independent and data-independent.

As in Chapter 3, we next let a, m, and r denote the computational costs of a single addition, multiplication, and square-root operation, respectively. We also assume that the cost of a division operation is m as well, and recall that

$$Cost(\text{DAS}) = 2(M-1)a + (M+3)m + m = 2(M-1)a + (M+4)m. \tag{4.28}$$

On the other hand, the cost of calculating the ASSB output $y[n]$ is dominated by the cost of inverting matrix $\mathbf{A}_s$ and involves $O(L^3)$ additions, $O(L^3)$ multiplications, $O(L)$ square-roots, and $O(1)$ divisions. More specifically, according to Table 4.1,

$$\begin{aligned} Cost(\text{ASSB}) \quad &= (\frac{L^3}{6} + M(L+2) + \frac{3L^2}{2} + \frac{7L}{3} - 4)a + \\ &\quad (\frac{L^3}{6} + M(L+1) + 2L^2 + \frac{29L}{6} + \frac{43}{6})m + \\ &\quad (L+1)r\,. \end{aligned} \tag{4.29}$$

Since $L \le M/2$, then the ratio $\frac{Cost(DAS)}{Cost(ASSB)}$ is bounded by $O(M^2)$.

Table 4.1: Computational cost of each ASSB-based beamforming step.

	Addition	Multiplication	Square Root
$\mathbf{A}_s = \mathbf{A}^H \mathbf{A}$	LM	$L(M-1)$	0
$\mathbf{G}\mathbf{G}^H$	$(L^3+3L^2+2L)/6$	$(L^3+6L^2+11L+7)/6$	$L+1$
$(\mathbf{G}\mathbf{G}^H)(\mathbf{A}_s^{-1}\mathbf{b})$ =	L^2+2L-2	L^2+4L+2	0
Total plus CF	$\frac{L^3}{6}+M(L+2)+\frac{3L^2}{2}+\frac{7L}{3}-4$	$\frac{L^3}{6}+M(L+1)+2L^2+\frac{29L}{6}+\frac{43}{6}$	$L+1$
$y[n]$ Output of DAS Plus CF	$2(M-1)$	$M+4$	0

Chapter 5

Evaluation Results

This chapter presents experimental images that have been generated using the FIELD-II simulation tool [13]. In the first section, we evaluate the performance of our hybrid GSC-based beamforming method (see Chapter 3) in comparison to the always-adaptive GSC. In the second section, we evaluate the performance of our hybrid ASSB-based beamforming method (see Chapter 4) in comparison to the always-adaptive ASSB. In our simulations, we applied the studied beamforming methods to two dissimilar sets of imaging data. The first set of data is an image of the 12-point phantom (see Chapter 2), using $M = 98$, $L = 49$, and $N = 1$, which is well-suited for analyzing the spatial resolution. The second set of data is an image of the point-scatterer-cyst phantom (see Chapter 2), using $M = 66$, $L = 33$, and $N = 2$, which is well-suited for analyzing the contrast.

5.1 Hybrid GSC-Based Beamforming

Figures 5.1 – 5.6 show the images generated by the FIELD-II simulation tool [13] using hybrid GSC-based beamforming with four different thresholds: $T_{CF} = 0.01$, 0.05, 0.1, and 0.15. Table 5.1 shows the percentage of computational savings achieved by our hybrid GSC-based beamforming in comparison to the always-adaptive GSC in both test cases: the 12-point phantom, and the point-scatterer-cyst phantom. Numerical entries of Table

5.1 are provided in the [MIN, MAX] format that respectively represent the minimum and the maximum savings based on the two limiting assumptions. We have obtained MIN assuming that a single square-root operation, a single multiplication, and a single addition have the same unit cost. On the other hand, we have obtained MAX assuming that a single square-root operation is 32 times costlier than a single multiplication, and the latter is 10 times costlier than a single addition. Such assumptions reflect a range of potential hardware implementations of the square-root, multiplication, and addition circuits [44]. The total count of each operation type was taken from Table 3.1, with the corresponding savings computed using Equation (3.8). One can see that the computational savings range from 57.4% (T_{CF} = 0.01) to 98.8% (T_{CF} = 0.15) for the 12-point phantom, and from 45.0% (T_{CF} = 0.01) to 73.4% (T_{CF} = 0.15) for the point-scatterer-cyst phantom. Next, we briefly discuss each test case individually.

Table 5.1: Hybrid GSC-based beamforming: computational savings in comparison to fully adaptive GSC-based beamforming.

Adaptive Beamforming Method + CF	Savings (%): 12-point phantom M = 98, L = 49, N = 1	Savings (%): point-scatterer-cyst phantom M = 66, L = 33, N = 2
GSC with T_{CF} = 0.01	[57.3340, 57.3801]	[44.9971, 45.0440]
GSC with T_{CF} = 0.05	[95.1995, 95.2760]	[58.9069, 58.9683]
GSC with T_{CF} = 0.1	[98.1849, 98.2638]	[69.4118, 69.4842]
GSC with T_{CF} = 0.15	[98.6841, 98.7634]	[73.3567, 73.4332]

12-Point Phantom: To assess the quality of the beamformed 12-point phantom image, we used the full width at half maximum (FWHM) as an indication of the resolution and the sidelobe energy E_{SL} as an indication of the contrast, both measured at the transmitter focusing point (60 mm). The sidelobe energy was calculated for attenuation level larger than 25 dB, which is a measure of the sensitivity to the artifacts [12]. Figure 5.1 shows the corresponding PSF at the 60-mm focus, and Table 5.2 shows the measured FWHM and E_{SL} values, where lower quantities are indicative of better-quality imaging. One can see that using T_{CF} = 0.1 or 0.15 results in the E_{SL} values of approximately -31 dB, approaching -28 dB of the DAS beamformer (see Table 5.2 and Figures 5.3 and 5.4).

Table 5.2: Hybrid GSC-based beamforming: FWHM, sidelobe energy E_{SL}, and mainlobe energy E_{ML} at the transmit focus (12-point phantom).

Adaptive Beamforming Method + CF	FWHM (mm)	E_{SL} (dB)	E_{ML} (dB)	E_{SL} / E_{ML} (dB)
DAS	0.6723	-28.3204	1.7925	-30.1129
Always-Adaptive GSC	0.3511	-37.1534	-1.2899	-35.8636
GSC with T_{CF} = 0.01	0.3512	-37.1476	-1.2898	-35.8579
GSC with T_{CF} = 0.05	0.3512	-36.5223	-1.2893	-35.2329
GSC with T_{CF} = 0.1	0.3533	-31.2100	-1.2598	-29.9502
GSC with T_{CF} = 0.15	0.3537	-30.9943	-1.2542	-29.7400

Therefore, we recommend using our hybrid GSC with a lower T_{CF} = 0.05, which yields the image shown in Figure 5.3 (also see Figure 5.4. and Table 5.2) that is of comparable quality with respect to the always-adaptive GSC. Meanwhile, the computational cost of beamforming that image using our hybrid approach is approximately 95% cheaper. Note that the FWHM = 0.3511 mm and E_{SL} = -37.153 dB of the always-adaptive GSC are not significantly affected by switching to the hybrid GSC with T_{CF} = 0.05 (FWHM = 0.3512 mm and E_{SL} = -35.522 dB). In comparison to the hybrid GSC with a lower T_{CF} = 0.01 (FWHM = 0.3512 mm and E_{SL} = -37.148 dB), using T_{CF} = 0.05 only slightly degrades the image quality but substantially increases the computational savings (from 57% to 95%).

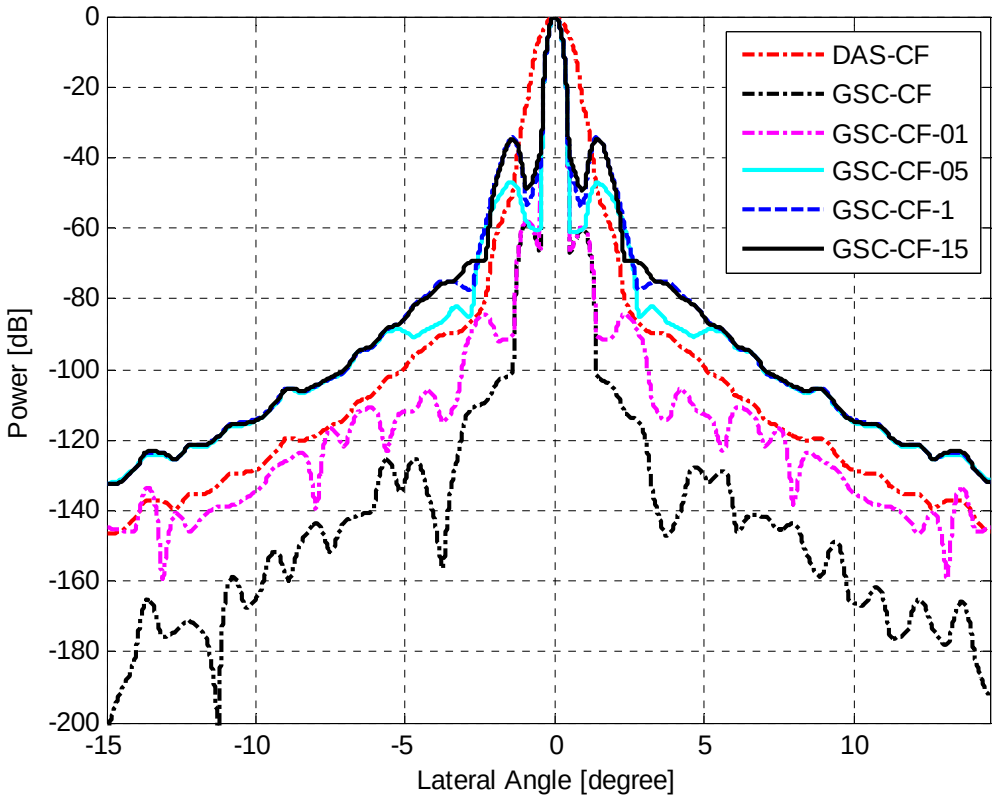

Figure 5.1: Hybrid GSC-based beamforming: PSF at transmit focus 60 mm.

Point-Scatterer-Cyst Phantom: The quality of the point-scatterer-cyst phantom images, shown in Figures 5.5 and 5.6, were assessed based on the contrast values C_{scat}, shown in Table 5.3 and calculated using Equation (2.3) applied to the rectangular regions indicated in Figure 5.2. Figure 5.2, which is obtained using the conventional delay-and-sum beamforming, shows the sampled rectangle areas used when computing the average log-compressed signal envelop. Note on order to have a better estimation of the background signal, the average is computed over six triangles [44].

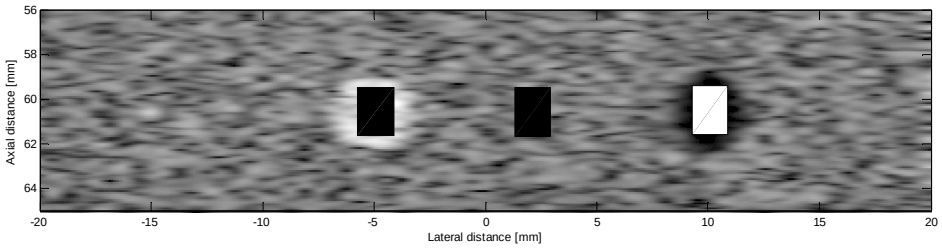

Figure 5.2: Sampled areas used for contrast computations: point-scatterer-cyst phantom obtained using DAS beamforming.

One can see that using T_{CF} = 0.1 or 0.15 results in C_{scat} in the range [3.18, 2.98], which is worse than C_{scat} in the range [3.43, 3.37] when using T_{CF} = 0.01 or 0.05. The always-adaptive GSC yields C_{scat} = 3.44, i.e., the hybrid GSC with T_{CF} = 0.05 is only 2% worse in terms of the contrast measure, but it offers about 59% computational savings (see Table 5.1). Therefore, we recommend using our hybrid GSC with T_{CF} = 0.05, which yields the image shown in Figure 5.6 that is of comparable quality with respect to the always-adaptive GSC. The DAS beamformer has much worse C_{scat} = 2.07, but interestingly it has the best value of the other contrast measure C_{water} (see Table 5.3), which is due to the lighter background (see Figures 5.5 and 5.6).

Table 5.3: Hybrid GSC-based beamforming: contrast with respect to the speckled background (point-scatterer-cyst phantom).

Adaptive beamforming method + CF	Mean signal in the background speckle $S_{in\_background}$	Contrast of the scattering region C_{scat}	Contrast of the water-filled region C_{water}
DAS	14.0267	2.0687	0.9848
Always-Adaptive GSC	6.2162	3.4383	0.9735
GSC with T_{CF} = 0.01	6.2946	3.4297	0.9756
GSC with T_{CF} = 0.05	6.5042	3.3696	0.9751
GSC with T_{CF} = 0.1	7.0950	3.1799	0.9679
GSC with T_{CF} = 0.15	7.9257	2.9806	0.9666

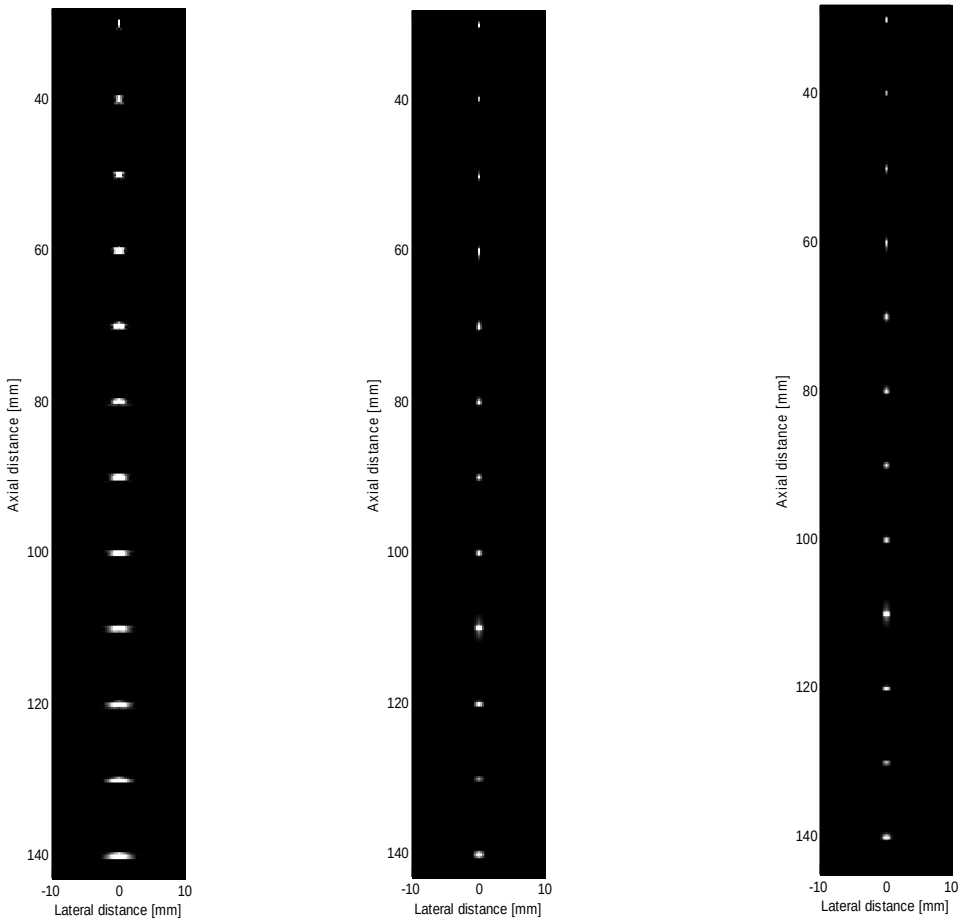

Figure 5.3: From left to right: 12-point phantom image obtained using DAS, fully adaptive GSC, and hybrid GSC with T_{CF} = 0.01.

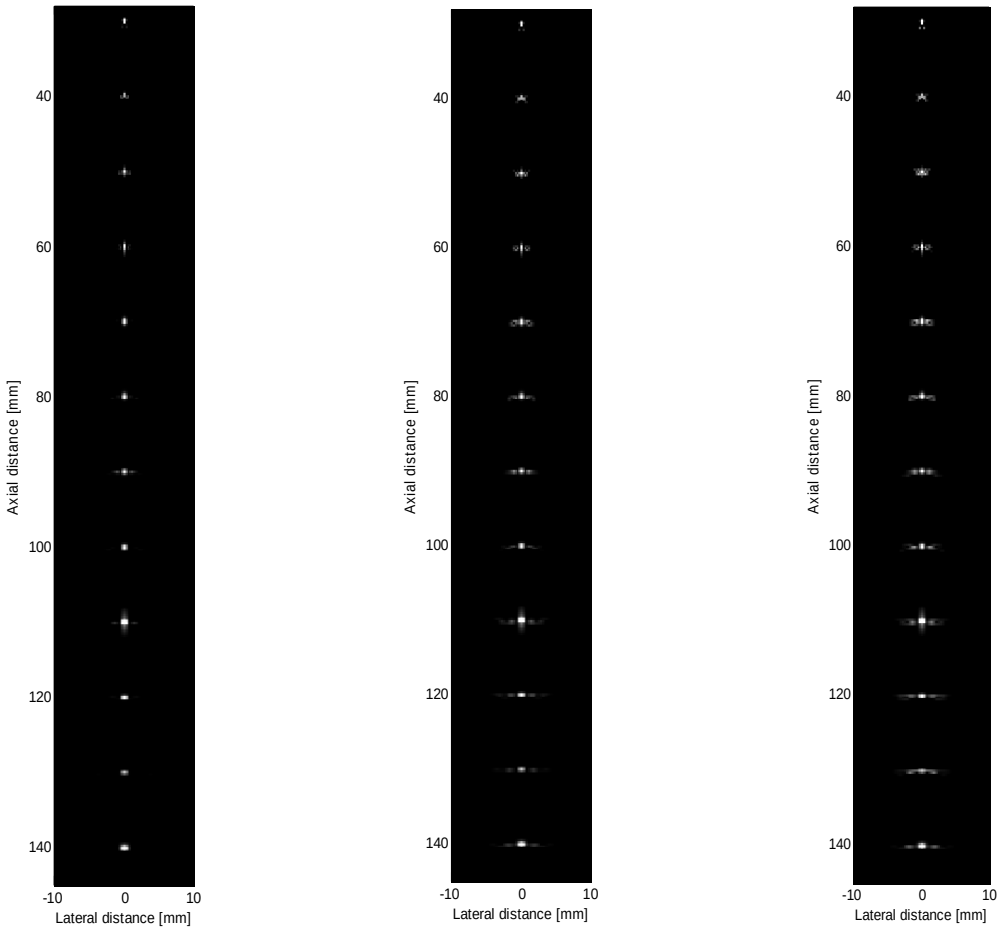

Figure 5.4: From left to right: 12-point phantom image obtained using hybrid GSC with T_{CF} = 0.05, hybrid GSC with T_{CF} = 0.1, and hybrid GSC with T_{CF} = 0.15.

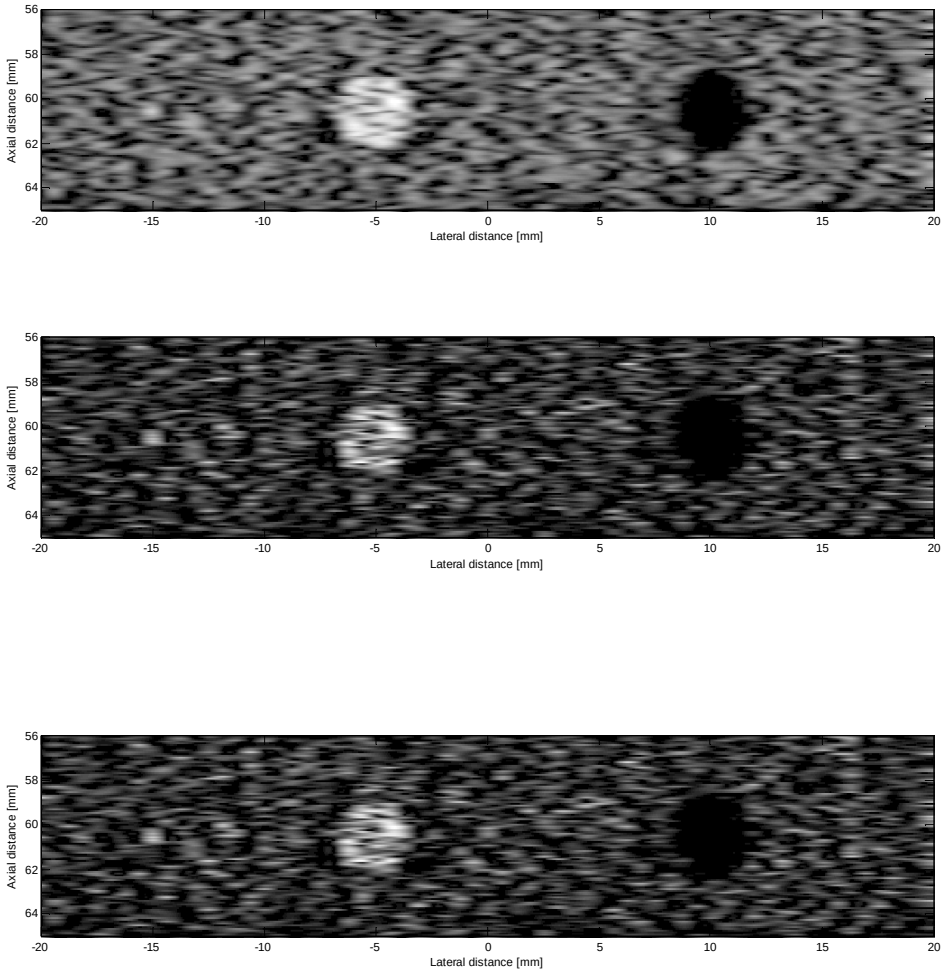

Figure 5.5: From top to bottom: point-scatterer-cyst phantom image obtained using DAS, always-adaptive GSC, and hybrid GSC with T_{CF} = 0.01.

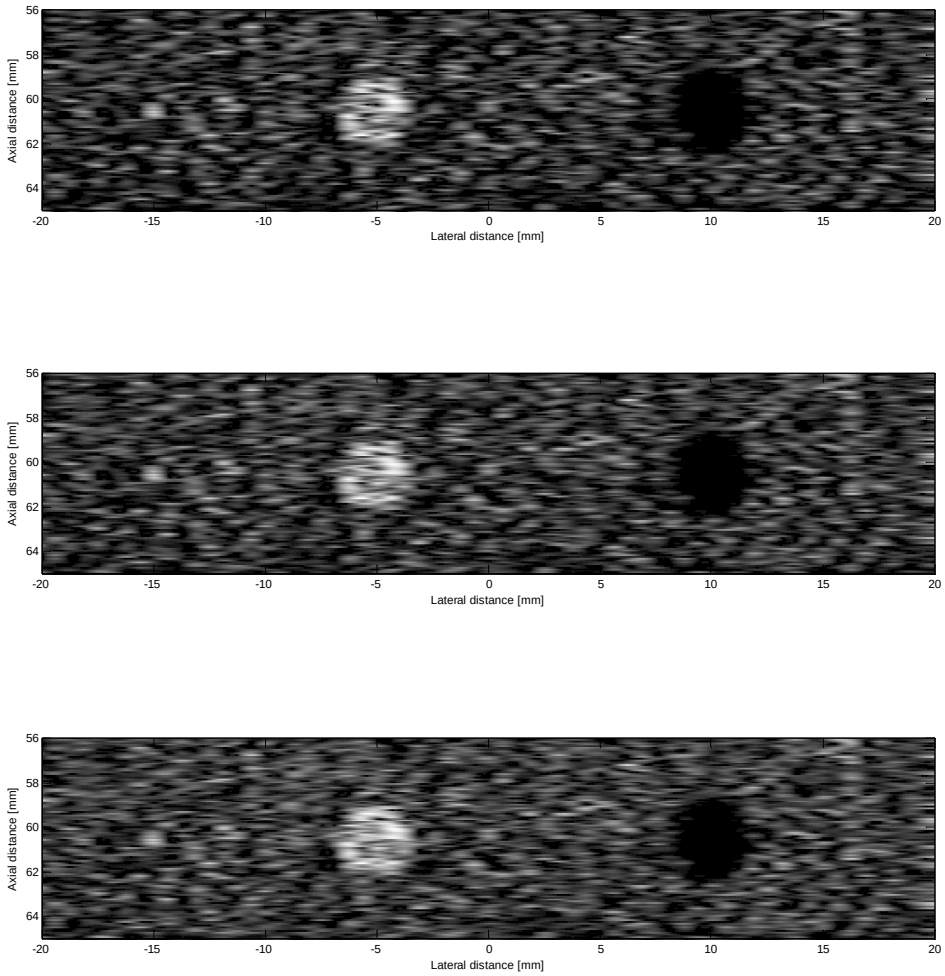

Figure 5.6: From top to bottom: point-scatterer-cyst phantom image obtained using hybrid GSC with T_{CF} = 0.05, hybrid GSC with T_{CF} = 0.1, and hybrid GSC with T_{CF} = 0.15.

5.2 Hybrid ASSB-Based Beamforming

Figures 5.7 – 5.11 show the images generated by the FIELD-II simulation tool [13] using hybrid ASSB-based beamforming with four different thresholds: T_{CF} = 0.01, 0.05, 0.1, 0.15. Table 5.4 shows the percentage of computational savings achieved by our hybrid ASSB in comparison to the always-adaptive ASSB in both test cases: the 12-point phantom, and the point-scatterer-cyst phantom. One can see that the computational savings range from 57.4% (T_{CF} = 0.01) to 98.8% (T_{CF} = 0.15) for the 12-point phantom, and from 45.0% (T_{CF} = 0.01) to 73.5% (T_{CF} = 0.15) for the point-scatterer-cyst phantom. These numbers are practically the same as in the case of our hybrid GSC. Next, we briefly discuss each test case individually.

Table 5.4: Hybrid ASSB-based beamforming: computational complexity in our test examples compared to always-adaptive ASSB beamforming.

Adaptive Beamforming Method + CF	Savings (%): 12-point phantom M = 98, L = 49, N = 1	Savings (%): point-scatterer-cyst phantom M = 66, L = 33, N = 1
ASSB with T_{CF} = 0.01	[57.3149, 57.3944]	[44.9544, 45.0724]
ASSB with T_{CF} = 0.05	[95.1678, 95.2998]	[58.8510, 59.0054]
ASSB with T_{CF} = 0.1	[98.1522, 98.2883]	[69.3460, 69.5280]
ASSB with T_{CF} = 0.15	[98.6512, 98.7881]	[73.2871, 73.4794]

12-Point Phantom: As in the case of our hybrid GSC, we used the same measures, i.e., FWHM and E_{SL}, to assess the quality of the ASSB-beamformed 12-point phantom image. Figure 5.7 shows the corresponding PSF at the 60-mm focus, and Table 5.5 shows the measured FWHM and E_{SL} values, where lower quantities are indicative of better-quality imaging. One can see that using T_{CF} = 0.15 results in E_{SL} = -29.93 dB, which is approximately 2 dB better than that of the DAS beamformer (see Table 5.5 and Figure 5.7). Decreasing the threshold value from 0.15 to 0.01 improves E_{SL} by less than 5% (from -29.93 dB to -31.36 dB). Our hybrid ASSB is less sensitive to T_{CF} variations than our hybrid GSC (see Table 5.2), for which decreasing T_{CF} from 0.15 to 0.01 improved E_{SL} by almost 20% (from -30.99 dB to -37.15 dB). The hybrid GSC clearly outperforms the hybrid ASSB, which is due to the superiority of GSC-based beamforming over ASSB-based beamforming (e.g., the always-adaptive GSC yields E_{SL} = -37.15 dB, while the always-adaptive ASSB yields E_{SL} = -31.38 dB). Both hybrids offer practically the same computational savings for the same T_{CF}. A similar conclusion can be drawn when comparing FWHM values of the two hybrids.

Due to a relatively low sensitivity of the hybrid ASSB to the threshold variations, we recommend using T_{CF} = 0.15 (to maximize the computational savings in comparison to the always-adaptive ASSB), which yields the image shown in Figure 5.8 that is of comparable quality with respect to the always-adaptive ASSB. However, the computational cost of beamforming those images using our hybrid approach is approximately 99% cheaper. Note that the FWHM = 0.3533 mm and E_{SL} = -31.38 dB of the always-adaptive ASSB are not significantly affected by switching to the hybrid ASSB with T_{CF} = 0.15 (FWHM = 0.3550 mm and E_{SL} = -29.93 dB). However, in comparison to the hybrid GSC with recommended T_{CF} = 0.01 or 0.05, the hybrid ASSB with recommended T_{CF} = 0.15 leads to substantially lower E_{SL} (i.e., approximately -30 dB versus -37 dB), but very close FWHM values (0.3512 mm versus 0.3550 mm), which can also be seen by visually comparing the images in Figures 5.1-5.2 (the hybrid GSC) with the image in Figures 5.7 and 5.8 (the hybrid ASSB). Note that visually the image produced by the hybrid GSC with T_{CF} = 0.15 (see Figure 5.3) appears to be worse than

the image produced by the hybrid GSC with T_{CF} = 0.15 (see Figure 5.8), even though the numerical measures of the image quality (see Tables 5.2 and 5.5) suggest otherwise. The comparative summary of the two hybrids with their recommended T_{CF} is given below.

- Hybrid CSG with T_{CF} = 0.05: ~95% savings, FWHM = 0.3512 mm, E_{SL} = -36.62 dB.
- Hybrid ASSB with T_{CF} = 0.15: ~99% savings, FWHM = 0.3550 mm, E_{SL} = -29.93 dB.

Table 5.5: Hybrid ASSB-based beamforming: FWHM, sidelobe energy E_{SL}, and mainlobe energy E_{ML} at the transmit focus (12-point phantom).

Adaptive Beamforming Method + CF	FWHM (mm)	E_{SL} (dB)	E_{ML} (dB)	E_{SL} / E_{ML} (dB)
DAS	0.6723	-28.3204	1.7925	-30.1129
Always-Adaptive ASSB	0.3533	-31.3803	-1.2589	-31.0068
ASSB with T_{CF} = 0.01	0.3533	-31.3619	-1.2588	-30.9878
ASSB with T_{CF} = 0.05	0.3533	-31.2763	-1.2584	-30.9021
ASSB with T_{CF} = 0.1	0.3551	-30.4154	-1.2101	-29.7734
ASSB with T_{CF} = 0.15	0.3550	-29.9330	-1.2341	-29.3127

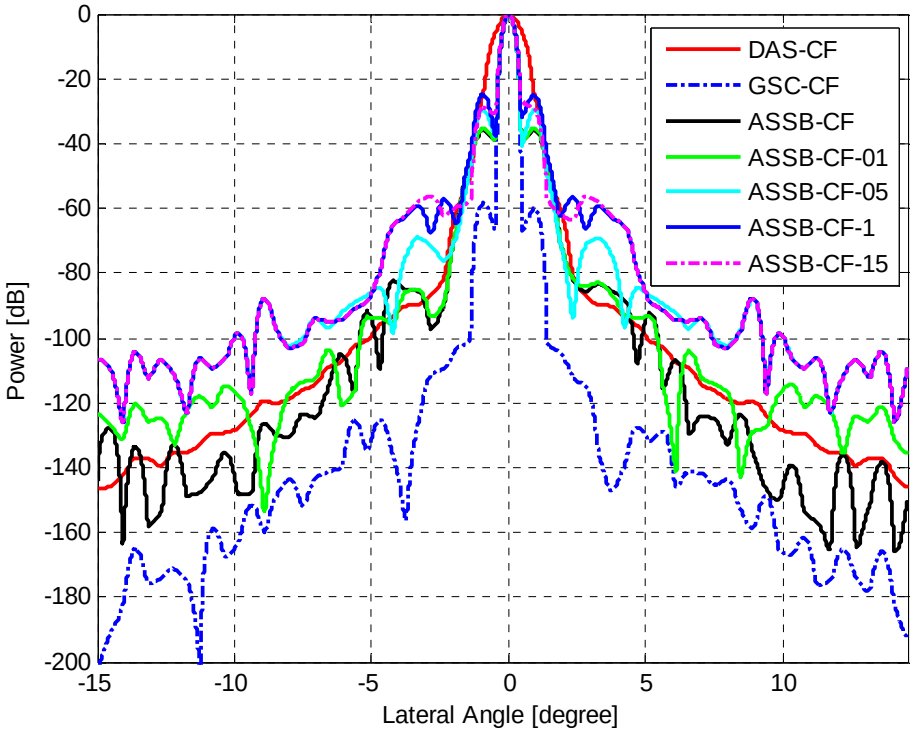

Figure 5.7: Hybrid ASSB-based beamforming: PSF at transmit focus 60 mm.

Point-Scatterer-Cyst Phantom: As in the case of our hybrid GSC, we used the same measure C_{scat} to assess the quality of the ASSB-beamformed point-scatterer-cyst phantom images, shown in Figures 5.10 and 5.11. One can see that using T_{CF} = 0.05, 0.1, or 0.15 results in C_{scat} of approximately 3.13, which is worse than C_{scat} = 3.21 when using T_{CF} = 0.01, or C_{scat} = 3.23 produced by the always-adaptive ASSB. In other words, the hybrid ASSB with T_{CF} = 0.15 is only 3% worse in terms of the contrast measure that the always-adaptive ASSB, but it offers 73% computational savings (see Table 5.4). Therefore, we

recommend using our hybrid ASSB with T_{CF} = 0.15, which yields the image shown in Figure 5.11 that is of comparable quality with respect to the always-adaptive ASSB (see Figure 5.10). Also, note that the hybrid ASSB exhibits lower sensitivity to the threshold variations than the hybrid GSC, for which the range of T_{CF} = [0.01, 0.15] resulted in the range of C_{scat} = [2.98, 3.43]. Interestingly, the hybrid ASSB with T_{CF} = 0.15 produces slightly better C_{scat} than that of the hybrid GSC with the same threshold (i.e., 3.13 versus 2.98). The comparative summary of the two hybrids with their recommended T_{CF} is given below.

- Hybrid CSG with T_{CF} = 0.05: ~59% savings, C_{scat} = 3.37.
- Hybrid ASSB with T_{CF} = 0.15: ~73% savings, C_{scat} = 3.13.

Table 5.6: Hybrid ASSB-based beamforming: contrast with respect to the speckled background (point-scatterer-cyst phantom).

Adaptive beamforming method + CF	Mean signal in the background speckle $S_{in\_background}$	Contrast of the scattering region C_{scat}	Contrast of the water-filled region C_{water}
DAS	14.0267	2.0687	0.9848
Always-Adaptive ASSB	6.9179	3.2275	0.9759
ASSB with T_{CF} = 0.01	6.9464	3.2135	0.9760
ASSB with T_{CF} = 0.05	7.0738	3.1320	0.9760
ASSB with T_{CF} = 0.1	7.0809	3.1266	0.9789
ASSB with T_{CF} = 0.15	7.0817	3.1260	0.9803

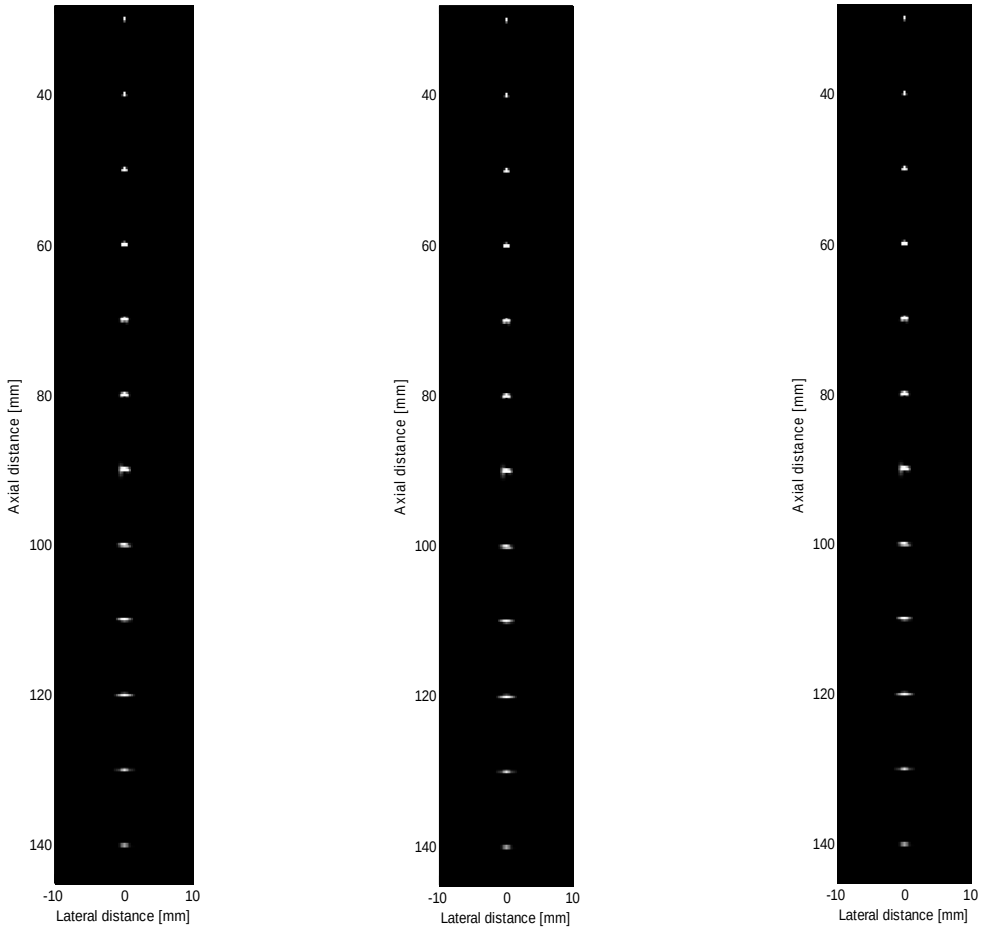

Figure 5.8: From left to right: 12-point phantom image obtained using always-adaptive ASSB, hybrid ASSB with T_{CF} = 0.01, and hybrid ASSB with T_{CF} = 0.05.

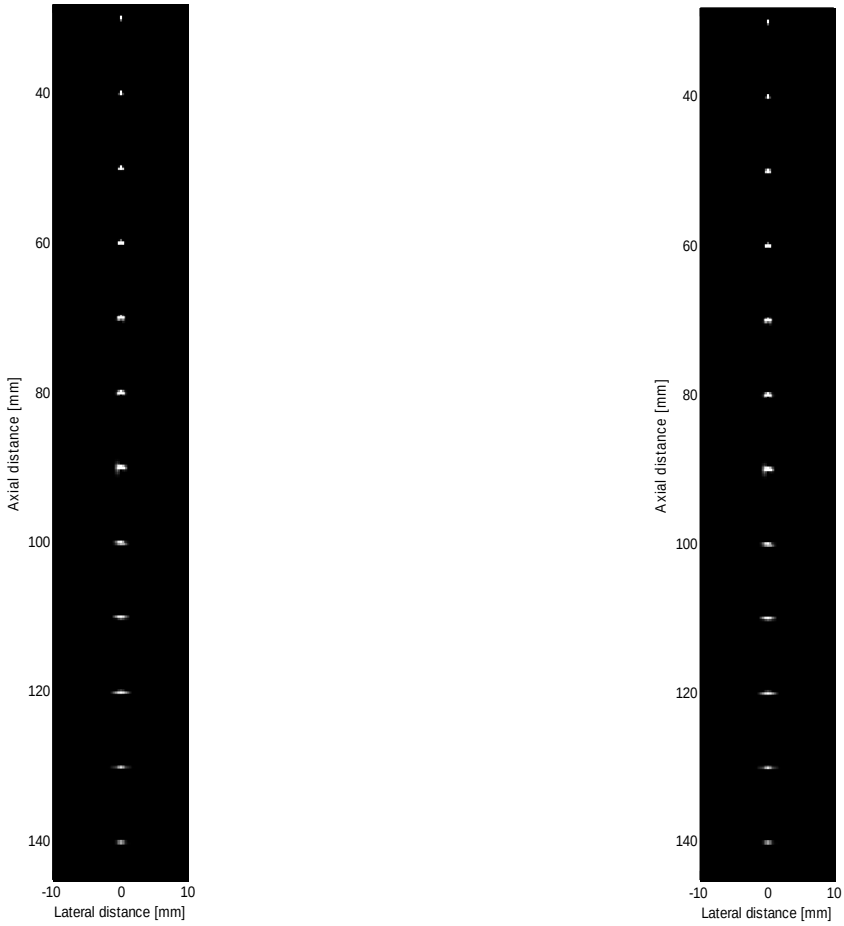

Figure 5.9: From left to right: 12-point phantom image obtained using hybrid ASSB with T_{CF} = 0.1, and hybrid ASSB with T_{CF} = 0.15.

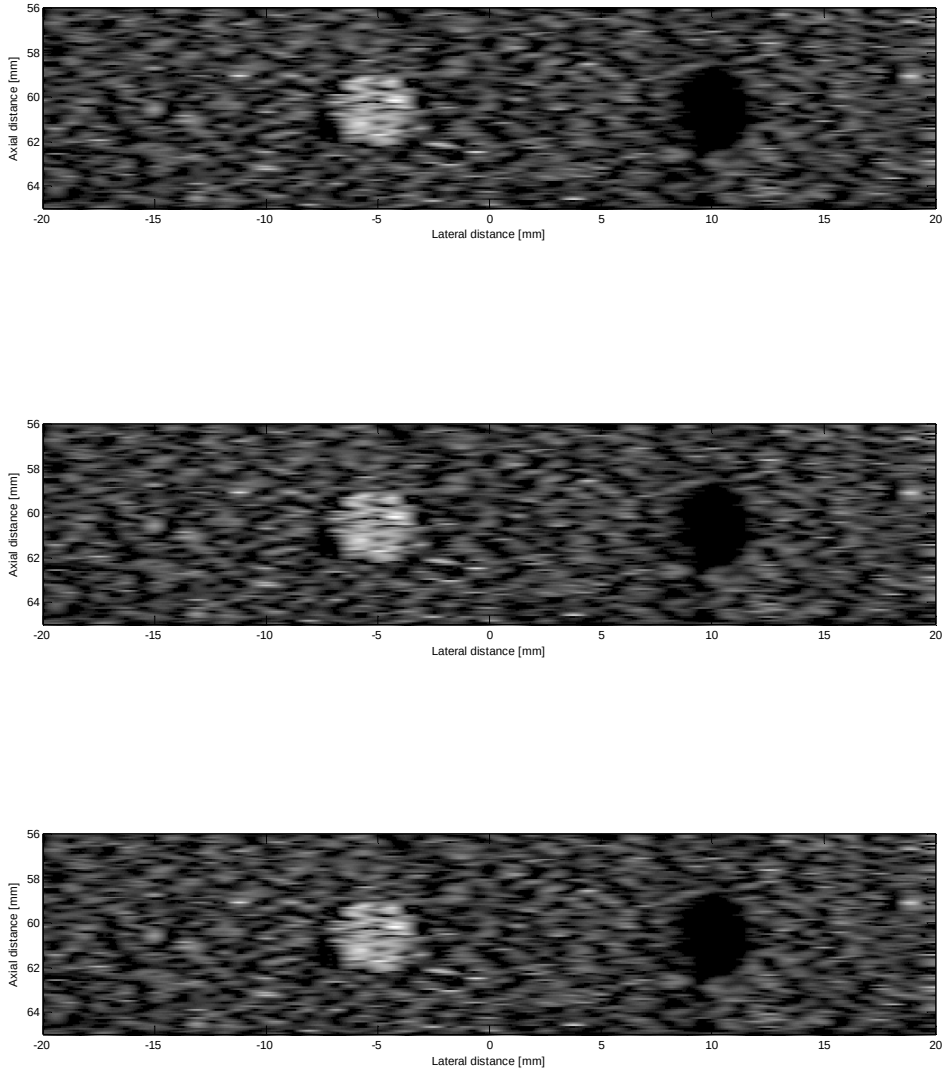

Figure 5.10: From top to bottom: point-scatterer-cyst phantom image obtained using always-adaptive ASSB, hybrid ASSB with T_{CF} = 0.01, and hybrid ASSB with T_{CF} = 0.05.

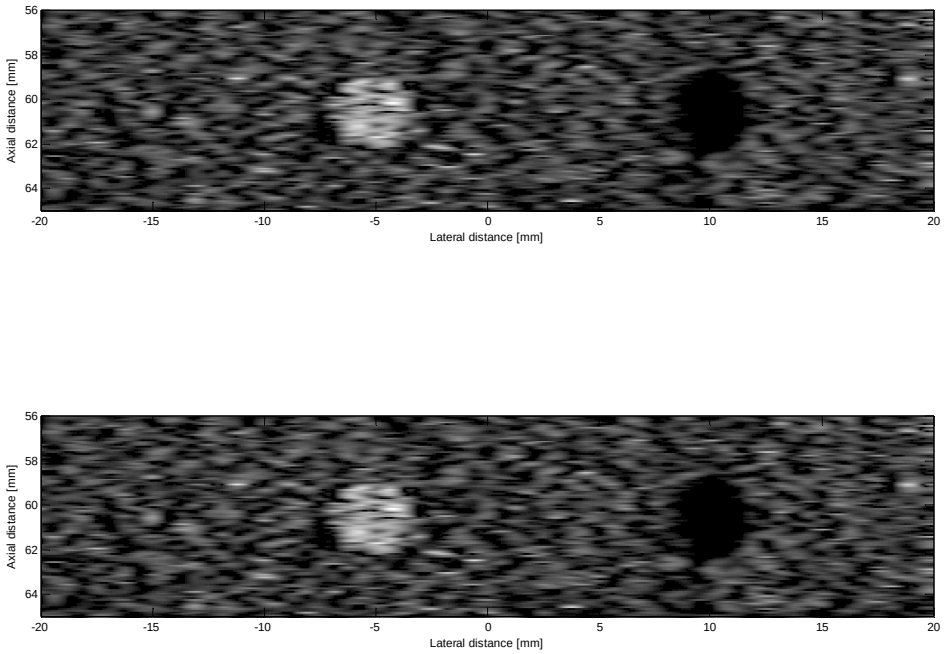

Figure 5.11: From top to bottom: point-scatterer-cyst phantom image obtained using hybrid ASSB with T_{CF} = 0.1 and hybrid ASSB with T_{CF} = 0.15.

Chapter 6

Conclusion and Future Work

In this chapter we briefly summarize our main results and outline several potential directions of future research and development efforts.

6.1 Conclusion

Adaptive beamforming has been demonstrated to yield significant improvements in resolution and contrast of ultrasound images in comparison to conventional DAS beamforming, as illustrated in this thesis and reported in the existing literature. However, adaptive beamformers impose a high computational load on the ultrasound system. To address this problem, we have explored a thresholding scheme that relies on the CF value to switch between low-quality low-complexity non-adaptive DAS beamforming (CF below the threshold value T_{CF}) and high-quality high-complexity adaptive GSC-based or ASSB-based beamforming (CF above the threshold value T_{CF}). Our simulation results (involving the ultrasound images of the 12-point phantom and the point-scatterer-cyst phantom) have shown that our hybrid GSC/DAS and ASSB/DAS beamformers can achieve 59-99% computational savings, in comparison to the respective always-adaptive beamforming methods. At the same time, they have been able retain the image quality

(i.e., resolution and contrast) comparable to that of produced by the always-adaptive beamformers. In other words, our results suggest that our simple thresholding scheme can be very effective in ultrasound imaging applications, as summarized in the tables below.

Table 6.1: 12-point phantom: performance summary of DAS, always-adaptive GSC, recommended hybrid GSC, always-adaptive ASSB, and recommended hybrid ASSB beamforming.

Beamforming method used	Resolution: FWHM	Degradation w.r.t. always-adaptive GSC/ASSB	Savings w.r.t. always-adaptive GSC/ASSB
DAS	0.6723 mm	~90%	~100%
Always-Adaptive GSC	0.3511 mm	0%	0%
GSC with T_{CF} = 0.05	0.3512 mm	0.03%	~95%
Always-Adaptive ASSB	0.3533 mm	0%	0%
ASSB with T_{CF} = 0.15	0.3550 mm	0.5%	~99%

Table 6.2: Point-scatterer-cyst phantom: performance summary of DAS, always-adaptive GSC, recommended hybrid GSC, always-adaptive ASSB, and recommended hybrid ASSB beamforming.

Beamforming method used	Contrast: C_{scat}	Degradation w.r.t. always-adaptive GSC/ASSB	Savings w.r.t. always-adaptive GSC/ASSB
DAS	2.0687	~40%	~100%
Always-Adaptive GSC	3.4383	0%	0%
GSC with T_{CF} = 0.05	3.3696	2.0%	~59%
Always-Adaptive ASSB	3.2275	0%	0%
ASSB with T_{CF} = 0.15	3.1260	3.1%	~73%

6.2 Future Work

Due to their low computational complexity, the hybrid beamformers presented in this thesis have a potential to enable online adaptive beamforming in ultrasound systems, as opposed to always-adaptive beamforming currently limited to off-line processing [30]. The future work can target either further reductions in the computational footprint of high-complexity high-quality beamforming, or further improvements in the image quality of low-quality low-complexity beamforming, with a goal of striking an appropriate data-dependent balance between the quality and complexity of a beamforming process. Some of our recommendations are outlined below.

- The data matrix used in ASSB-based beamforming has a special structure that may allow for faster matrix inversion computations, which is the dominant cost factor. An adaptive beamformer (GSC or ASSB) may also try to use approximate matrix inverses (e.g., obtained by a conjugate gradient method using only a small number of iterations), thus reducing its computational complexity.
- As an alternative to the GSC and ASSB, one can investigate the performance of an appropriate thresholding scheme applied to the beamspace and the principal-component beamformers that have also been used in ultrasound imaging. One can also study the applicability of thresholding to aperture sizing.
- Rather than fixing the coherence-factor threshold T_{CF} at a certain value, one can explore various policies of adjusting it dynamically, e.g., based on some estimated spatial or temporal characteristics of the image data being processed.
- There are two very important problems that have not been addressed in this thesis: broadband beamforming and robust beamforming. Using a broadband or robust beamformer will significantly increase the computational load. A future study of reduced-complexity hybrids for such beamformers is likely to be very valuable.

Bibliography

[1] T. Szabo, *Diagnostic Ultrasound Imaging: Inside Out*. MA: Elsevier, 2004.

[2] Texas Instruments, “Ultrasound System,” 2009, http://focus.ti.com/docs/solution/folders/print/346.html.

[3] R. Cobbold, *Foundations of Biomedical Ultrasound*. NY: Oxford University Press, 2007.

[4] F. Harris, "On the use of windows for harmonic analysis with the discrete Fourier transform," *Proceedings of the IEEE* , vol.66, no.1, pp. 51- 83, Jan. 1978.

[5] H. L. V. Trees, *Detection, Estimation, and Modulation Theory IV: Optimum Array Processing*. New York: Wiley, 2002.

[6] J. A. Jensen, Medical ultrasound imaging. *Progress in Biophysics and Molecular Biology*, 93:153–165, 2007.

[7] R. G. Lyons, *Understanding Digital Signal Processing*. NJ: Prentice Hall, 2004.

[8] J.-F. Synnevag, C. I. C. Nilsen, and S. Holm, "P2B-13 Speckle Statistics in Adaptive Beamforming," *Ultrasonics Symposium, 2007. IEEE* , vol., no., pp.1545-1548, 28-31, October 2007.

[9] T. Shah and T. Kailath, "Adaptive beamforming for coherent signals and interference," *Acoustics, Speech and Signal Processing, IEEE Transactions on* , vol.33, no.3, pp. 527- 536, Jun 1985.

[10] M. Sasso and C. Cohen-Bacrie, "Medical ultrasound imaging using the fully adaptive beamformer," in *Proceedings ICASSP*, vol.2, pp. 489- 492, March 2005.

[11] B. Widrow, K. Duvall, R. Gooch, and W. Newman, "Signal cancellation phenomena in adaptive antennas: Causes and cures," *Antennas and Propagation, IEEE Transactions on* , vol.30, no.3, pp. 469- 478, May 1982.

[12] K. W. Hollmand, K. W. Rigby, and M. O'Donnell, "Coherence factor of speckle from a multi-row probe," *Ultrasonics Symposium, 1999. Proceedings. 1999 IEEE* ,vol.2, no., pp.1257-1260 vol.2, 1999.

[13] J. Jensen, "Field II Simulation Program," 2008, http://server.elektro.dtu.dk/ personal/jaj/field.

[14] J. Jensen, "Field: A program for simulating ultrasound systems," *10th Nordic-Baltic Conference on Biomedical Imaging Published in Medical and Biological Engineering and Computing*, vol. 34, pp. 351–353, 1996.

[15] J. Jensen and N. Svendsen, "Calculation of pressure fields from arbitrarily shaped, apodized, and excited ultrasound transducers," *Ultrasonics, Ferroelectrics and Frequency Control, IEEE Transactions on* , vol.39, no.2, pp.262-267, March 1992.

[16] D. Johnson and D. Dudgeon, *Array Signal Processing*: *Concepts and Techniques.* Upper Saddle River, NJ*:* Prentice-Hall*,* 1993.

[17] B. V. Veen and K. Buckley, "Beamforming: a versatile approach to spatial filtering," *ASSP Magazine, IEEE* , vol.5, no.2, pp.4-24, April 1988.

[18] J. Capon, "High-resolution frequency-wavenumber spectrum analysis," *Proceedings of the IEEE* , vol.57, no.8, pp. 1408- 1418, August 1969.

[19] L. Griffiths and C. Jim, "An alternative approach to linearly constrained adaptive beamforming," *Antennas and Propagation, IEEE Transactions on* , vol.30, no.1, pp. 27- 34, Jan 1982.

[20] O. L. Frost, "An algorithm for linearly constrained adaptive array processing," *Proceedings of the IEEE* , vol.60, no.8, pp. 926- 935, August 1972.

[21] J. S. Goldstein and I. S. Reed, "Reduced-rank adaptive filtering," *Signal Processing, IEEE Transactions on* , vol.45, no.2, pp.492-496, February 1997.

[22] D. Guenther and W. Walker, "Optimal apodization design for medical ultrasound using constrained least squares part I: theory," *Ultrasonics, Ferroelectrics and Frequency Control, IEEE Transactions on* , vol.54, no.2, pp.332-342, February 2007.

[23] D. Guenther and W. Walker, "Optimal apodization design for medical ultrasound using constrained least squares part II simulation results," *Ultrasonics, Ferroelectrics and Frequency Control, IEEE Transactions on* , vol.54, no.2, pp.343-358, February 2007.

[24] K. Ranganathan, M. Santy, T. Blalock, J. Hossack, and W. Walker, "Direct sampled I/Q beamforming for compact and very low-cost ultrasound imaging," *Ultrasonics, Ferroelectrics and Frequency Control, IEEE Transactions on* , vol.51, no.9, pp.1082-1094, September 2004.

[25] K. Ranganathan and W. Walker, "A novel beamformer design method for medical ultrasound. Part I: Theory," *Ultrasonics, Ferroelectrics and Frequency Control, IEEE Transactions on* , vol.50, no.1, pp.15-24, January 2003

[26] K. Ranganathan and W. Walker, "A novel beamformer design method for medical ultrasound. Part II: Simulation results," *Ultrasonics, Ferroelectrics and Frequency Control, IEEE Transactions on* , vol.50, no.1, pp.25-39, January 2003.

[27] C. Seo and J. Yen, "Sidelobe suppression in ultrasound imaging using dual apodization with cross-correlation," *Ultrasonics, Ferroelectrics and Frequency Control, IEEE Transactions on* , vol.55, no.10, pp.2198-2210, October 2008.

[28] J-F. Synnevag, A. Austeng, and S. Holm, "A low-complexity data-dependent, beamformer," *Ultrasonics, Ferroelectrics and Frequency Control, IEEE Transactions on* ,vol.58, no.2, pp.281-289, February 2011.

[29] Z. Wang, J. Li, and R. Wu, "Time-delay- and time-reversal-based robust capon beamformers for ultrasound imaging," *Medical Imaging, IEEE Transactions on* , vol.24,no.10, pp.1308-1322, October 2005.

[30] F. Vignon and M. Burcher, "Capon beamforming in medical ultrasound imaging with focused beams," *Ultrasonics, Ferroelectrics and Frequency Control, IEEE Transactions on* , vol.55, no.3, pp.619-628, March 2008.

[31] J-F. Synnevag, A. Austeng, and S. Holm, "Adaptive Beamforming Applied to Medical Ultrasound Imaging," *Ultrasonics, Ferroelectrics and Frequency Control, IEEE Transactions on* , vol.54, no.8, pp.1606-1613, August 2007.

[32] B. M. Asl and A. Mahloojifar, "Eigenspace-based minimum variance beamforming applied to medical ultrasound imaging," *Ultrasonics, Ferroelectrics and Frequency Control, IEEE Transactions on* , vol.57, no.11, pp.2381-2390, November 2010.

[33] B. M. Asl and A. Mahloojifar, "Contrast enhancement and robustness improvement of adaptive ultrasound imaging using forward-backward minimum variance beamforming," *Ultrasonics, Ferroelectrics and Frequency Control, IEEE Transactions on* , vol.58, no.4, pp.858-867, April 2011.

[34] S . Park, A. B. Karpiouk, and S. R. Aglyamov, "Adaptive beamforming for *2008.* photoacoustic imaging using linear array transducer," *Ultrasonics Symposium, 2008. IUS IEEE* , vol., no., pp.1088-1091, 2-5 November 2008.

[35] S .-L. Wang and P.-C. Li, "MVDR-based coherence weighting for high-frame-rate adaptive imaging," *Ultrasonics, Ferroelectrics and Frequency Control, IEEE Transactions on* , vol.56, no.10, pp.2097-2110, October 2009.

[36] C.-I.C. Nilsen and S. Holm, "Wiener beamforming and the coherence factor in ultrasound imaging," *Ultrasonics, Ferroelectrics and Frequency Control, IEEE Transactions on* , vol.57, no.6, pp.1329-1346, June 2010.

[37] J. A. Mann and W. F. Walker, "A constrained adaptive beamformer for medical ultrasound: initial results," *Ultrasonics Symposium, 2002. Proceedings. 2002 IEEE* ,vol.2, no., pp. 1807- 1810 vol.2, 8-11 October 2002.

[38] I. Holfort, F. Gran, and J. Jensen, "Broadband minimum variance beamforming for ultrasound imaging," *Ultrasonics, Ferroelectrics and Frequency Control, IEEE Transactions on* , vol.56, no.2, pp.314-325, February 2009.

[39] F. Viola and W. Walker, "Adaptive signal processing in medical ultrasound beamforming," *Ultrasonics Symposium, 2005 IEEE* , vol.4, no., pp. 1980- 1983, 18- 21, September 2005.

[40] F. Viola, M. Ellis, and W. Walker, Time-Domain Optimized Near-Field Estimator for Ultrasound Imaging: Initial Development and Results," *Medical Imaging, IEEE Transactions on* , vol.27, no.1, pp.99-110, January 2008.

[41] R. Bethel, B. Shapo, and H. Van Trees, "Single snapshot spatial processing: optimized and constrained," *Sensor Array and Multichannel Signal Processing Workshop Proceedings, 2002* , vol., no., pp. 508- 512, 4-6 August 2002.

[42] M. Ali and P. Schreib, "Adaptive single snapshot beamforming: a new concept for the rejection of nonstationary and coherent interferers," *Signal Processing, IEEE Transactions on* , vol.40, no.12, pp.3055-3058, December 1992 .

[43] C.-I.C. Nilsen, I. Hafizovic, "Beamspace adaptive beamforming for ultrasound imaging," *Ultrasonics, Ferroelectrics and Frequency Control, IEEE Transactions on* , vol.56, no.10, pp.2187-2197, October 2009.

[44] S. Khezerloo, " *Gradient-Driven and Reduced-Rate Beamforming for Biomedical Ultrasound*" MASc. thesis, University of Victoria, Victoria, BC, 2009.

[45] R. Hunger, "Floating Point Operations in Matrix-Vector Calculus," Munich University of Technology, Tech. Rep. TUM-LNS-TR-05-05, October 2005.

[46] T.J. Shan, M. Wax, and T. Kailath, "On spatial smoothing for direction-of-arrival estimation of coherent signals," *Acoustics, Speech and Signal Processing, IEEE Transactions on* , vol.33, no.4, pp. 806- 811, August 1985.

[47] C. L. Lawson and R. J. Hanson, *Solving Least Squares Problems.* Englewood Cliffs, NJ: Prentice-Hall, 1974.

[48] A. Antoniou and W. Lu, *Practical Optimization*. NY: Springer, 2007.

[49] Gilbert Strang, The fundamental theorem of linear algebra, *American Mathematical Monthly*, vol.100, no.9, pp. 848 - 859, November 1993.

[50] S. Khezerloo and D. Rakhmatov, "Gradient-driven beamforming for biomedical ultrasound," in *Engineering in Medicine and Biology Society, Annual International Conference of the IEEE*, 2009, pp. 444-450, 3-6 September 2009

[51] L. Hall, K. E. Thomenius, L. J. Thomas II, and K. W. Rigby, "*Method and apparatus for coherence imaging,*" U.S. Patent 6071240, June 6, 2000.

Appendix A

FIELD-II Simulation Tool

FIELD-II [13-15] is a software program used for simulating all types of linear medical ultrasound systems. It uses linear acoustic models and the spatial impulse response to simulate the transducer pressure field and the backscattered field from a finite number of point scatterers. It provides an accurate and efficient approach of calculating all types of fields such as emitted and pulsed with all possible transducer geometries. The program is capable of simulating all image types such as cyst phantoms, artificial human phantoms and flow imaging phantoms. The FIELD-II has been developed by Dr. Jørgen Arendt Jensen, and it can be downloaded free of charge and from the program's website at the Technical University of Denmark [13]. The program's website has a number of examples that provides the starting point for simulating point spread functions, intensity calculation, B-mode images, and color flow imaging. The program consists of pre-compiled C routines and a number of Matlab m-functions. There are three types of the Matlab m-functions which are used for initializing the program, defining and manipulating the transducers, and performing the calculations. All the calculations are performed by the C routines and can be called directly using the Matlab m-functions.

After the initialization step, the scatterers' positions and amplitude are first generated and stored in a separate file to be called during the generation of the scan lines. In order to image any region of interest, the region is scanned using number of lines depending on the type of the data acquisition (for example, linear or phased arrays, as we used in our simulations). Each scan line is saved in a separate file for further processing. During the scanning process, fixed delay focusing and apodization are applied on the transmit side and dynamic focusing and fixed or dynamic apodization are applied at the receive side. In

the case of the 12-point phantom, the scatterers' amplitudes were set to one. In the case of the point-scatterer-cyst phantom, a collection of point scatterers were randomly positioned within a $50\times10\times20$-mm^3 region to generate the speckled background. The random point scatterers' amplitudes were determined by the Gaussian distribution. If, however, the point scatterers were in the water-filled cyst, their amplitudes were set to zero. In the other hand, if they were in the highly scattering region, their amplitudes were multiplied by 10. The point target's amplitude was set to 20.